Impact of Land-Climate Interaction on Thermo-Hydro-Mechanical based Stability Assessment of Varved Glacial Slopes

Deepali Anand[1], Arindam Dey[1*], Ravi Karangat[1]

[1]Indian Institute of Technology Guwahati, Guwahati-781039, Assam, India
*Corresponding author: arindamdeyiitg16@gmail.com

Abstract

The increasing average global temperatures are transforming the permafrost regions into seasonally frozen areas, thereby pushing the active layer deeper into the ground and leading to a rise in inexplicable glaciatic geohazards. Although the glaciated Himalayan regions of India are becoming more vulnerable to such events, cold region geotechnical studies remain nearly unattended. This research attempts to evaluate the complex consequences of hydrological changes on the stability of slopes and water balance through numerical modeling using the finite element (FE) technique. The real-time climate data from Tawang, Arunachal Pradesh, is chosen which prevalently experiences sub-zero temperatures in the eastern Himalayan belt. In accordance to various thermal regimes and hydrological conditions common to this region, this study effect of only rainfall water infiltration (RW), water infiltration from both rain and snowmelt (RW+SW), and the complementary influence water migration due to soil temperature gradient [T(RW+SW)] on the slope stability, water infiltration, and runoff dynamics of sloping terrain. Numerical assessment of the stability of both homogeneous and multi-couplet varve slope profiles are carried out. The influence of Red soil-Black soil (RS-BS) laminae (2, 4, 8 and 16 in numbers) as well as the slope inclination (25° - 45°) on the hydrogeological response of the layered slopes are delineated. It is conclusively understood that stability of slopes, water infiltration and runoff are strongly influenced by surficial soil couplet directly interacting with the atmosphere; expectedly, the slope inclination angle and the number of laminae also plays substantial role in the stability and temporal dynamics of pore-water pressure within the slopes. Slopes with RS as the topmost layer are found to evidently fail earlier than those with BS as the topmost layer; for the latter case, the area of soil involved in slope failure is comparatively lesser. In any sequential arrangement, the area of soil involved in slope failure increases with the increase in laminae. Slopes with RS as the topmost layer are observed fail quicker under the freeze-thaw phenomenon. The time to the onset of slope failure is found to be comprehensively linked with the time to attain the maximum cumulative net infiltration.

Keywords: Glacial Slope Stability, Reconstituted Varved Clays, Freezing and Thawing, Land-Climate Interaction, Thermo-Hydro-Mechanical Coupling

1. Introduction

The stability of slopes is a critical concern in Indian Himalayan region, particularly given the prevalence of landslides and their potential to cause significant societal and economic damage [1]. The Indian Himalayan region is infamous for slope instability problems due to its structure, geology, and dynamic regional climate [2]. Severe rainfall, snow melt, tectonic activities and human intervention in the region are the main causes of the instability of the slopes [3, 4]. While the stability of slopes under normal temperature conditions is well-documented, studies focusing on cold regions remain scarce. Although several studies on rainfall-induced slope failures are frequently reported in the literature, there are only few that incorporate and consider water from snowmelt, sub-zero temperatures, and the freezing and thawing in sloping ground. The increased frequency and unpredictability of landslides in the Himalayan regions have motivated researchers to investigate the complex mechanisms behind these events [5-7].

Most studies on slope stability reported in the literature focus on homogeneous soil profiles; however, real-world scenarios often involve slopes composed of heterogeneous soils with layer-by-layer deposition [8]. Weak soil layers within the slopes often trigger landslides under conditions of water infiltration [9]. Previous researches have also emphasized the importance of considering soil layering in slope stability studies [10-14]. Additionally, there are limited studies on water balance in Indian Himalayan regions that incorporate the contributions from both water infiltrations into slope profiles and runoff. Understanding the impact of infiltrated water on slope stability and runoff is crucial for designing effective slope stabilization measures and managing water resources in mountainous regions prone to hydrological hazards and landslide events. This study addresses these gaps by examining stability of slopes in homogeneous and multi-couplet reconstituted varved clay slope profiles under three climatic conditions. These climatic conditions include water consideration from rain only (RW), rain combined with snowmelt (RW+SW), and rain with snowmelt considering temperature gradient along the depth of the soil [T(RW+SW)]. The temperature gradient along the depth of the soil induces water migration and facilitates freezing and thawing in sloping ground.

Several researchers have conducted stability analyses of layered slopes. Dai *et al.* [5] conducted parametric stability analysis on two-layered slope profiles, and observed that the thickness of the lower layer significantly influenced the Factor of Safety (FoS) of slopes. Chatterjee and Murali Krishna [6] carried out numerical modelling to analyze slope stability in homogeneous and layered soils, and found that slip surfaces remain confined in the top layer when the foundation soil is stiffer. Sarkar and Chakraborty [7] demonstrated that presence of a stronger soil layer over weaker ones enhanced slope stability, especially in steep slopes. Wu *et al.* [14] conducted rainwater infiltration experiments, and noted significant variations in pore-water pressure and water content along the depth of layered slopes. Tang *et al.* [15] explored water infiltration characteristics and failure modes in layered and homogenous soil slope. The authors reported occurrence of soil piping in layered soil slopes and surface sliding in homogeneous soil slopes. Irfan *et al.* [16] conducted stability analyses 625 slopes comprising layered excavations to propose a correlation expression for assessing the FoS of slopes with similar configurations. The slope consisted of a vertical cut clay layer resting at the top of a sandy slope with a horizontal interface. The analysis was performed by varying the cohesion of the clay layer, the angle of internal friction of the sand layer, the thickness ratio (the ratio of the height of the clay layer to the sand layer) and the inclination of the sand layer. apart from the shear strength parameters of the layered soil and inclination of the underlying soil, the thickness ratio of the layers also plays an influencing role on the slope stability.

Weng [17] observed a significant drop in FoS of layered soil slopes after breakthrough, compared to homogeneous soil slopes. Few researchers have conducted stability analyses of slopes while considering freezing and thawing effects. However, these studies, which include freeze-thaw effects, were carried out on homogeneous soils. For example, Wang *et al.* [18] found that FoS increased during freezing but decreased during thawing due to the expansion of the yield zone. Li and Chen [19] observed a linear decrease in FoS with increasing freeze-thaw depth. Chen *et al.* [20] developed a method to predict landslides by analyzing vertical displacement and the effects of moisture content on FoS. All the layered slope stability studies discussed above typically consider slopes formed by horizontally deposited soil; however, in reality, the layers in slopes often exist parallel to the ground surface [21]. Moreover, none of these studies addressed layered slopes in cold regions or the contributions of volume of water to infiltration and runoff. While studies on the slope stability of layered soils often focus on one or two layers, as evident from the above discussed literature, natural slopes frequently consist of multiple layers. The present study addresses these complexities by considering multiple layers parallel to the sloping ground and comparing how slope stability, infiltration, and runoff are affected when freezing and thawing are incorporated into the stability analysis of slopes.

This study uses meteorological data from Tawang, a district in the Northeastern state of Arunachal Pradesh, India. The Himalayas in Northeast India are highly vulnerable to landslides and experience chronic economic losses worth billions of rupees due to a wide range of landslide issues [22]. Compared to other regions in the Indian Himalayan belt, the Northeastern Indian Himalayas have seen a dearth of research on slope stability analysis [23]. The scarcity of research in the region is primarily attributed to the remoteness of this region and its challenging terrains [24, 25]. Varved clays have been reported as common soil deposits in glacial environments [26-31] and have been observed in glaciated Indian Himalayan regions as well [32-36].

The current study involves analyzing the FoS against slope failure, cumulative net infiltration, and cumulative runoff in both homogenous and multi-couplet reconstituted varved clay slope profiles. The reconstituted varved laminae structure consists of alternately and repetitively arranged Red Soil (RS) and Black Soil (BS) to replicate the actual varved clay laminae. Homogenous slopes constitute separately of RS and BS. The study is carried out at five different slope inclination angles of 25°, 30°, 35°, 40°, and 45°. This study addresses a broad range of research gaps and enhances the understanding of complex interactions among soil composition, sequential arrangement, and the number of laminae on slope stability, infiltration, and runoff under different climatic conditions through FE numerical modelling.

2. Materials and Methodology

RS and BS used in the present study were obtained from the vicinity of the IIT Guwahati campus. Various geotechnical tests were carried out to determine the material characterization of these soils and obtain input parameters for numerical modeling, which are discussed in detail in Sections 2.1 and 2.2, respectively.

2.1 Material Characterization of RS and BS used as Constituent Laminae

RS and BS used in this study represent two soils that constitute the two laminae of actual varved clay. The selection of RS and BS for this representation was based on a preliminary geotechnical investigation conducted in the laboratory. These geotechnical investigations included determining of Atterberg Limits [37] and obtaining Particle Size Distribution [38]. The geotechnical analysis revealed that RS can effectively represent the light-coloured, silt-dominant laminae found in actual varved clays, while BS can serve as a representative of the darker, clay-dominant laminae. The laboratory test based basic geotechnical parameters is listed in Table 1, and are consistent with the characteristics of actual varved clays documented in the literature [39-46]. Table 1 also lists other parameters obtained from laboratory tests, such as the magnitudes of specific gravity [47], compaction characteristics [48] and shear strength parameters of the soils. The shear strength parameters were obtained from Direct Shear Tests (DST) conducted following ASTM D3080/D3080M [49], and are utilized as input parameters during slope stability analysis. As the multi-laminae slopes are analysed for their stability, which would be primarily triggered through translational slides through the interface of the laminar, DST is adjudged a suitable and relevant technique to assess the shear strength parameters of the soil specimens. As per the USGS classification system and based on the Atterberg's limit confirmatively assessed for RS and BS, they have been classified as ML (low plasticity silts) and CH (high plasticity clays), respectively. The classification also conforms to the particle size distribution assessed for the soils. However, conventionally, based on the classification, BS is expected to exhibit higher cohesion compared to RS. However, for the present study, the observation has been found to be otherwise, and the same has been confirmed through repetition of the direct shear test experiments on the samples with optimum moisture content-maximum dry density (OMC-MDD) condition. Being direct shear test, it might be noted that the cohesion in this case can be more aptly termed as 'apparent cohesion' (as mentioned in Table 1). As explicable, the angle of internal friction for the BS has turned out to be lower than that of RS. However, the apparent cohesion of BS being lower than that of RS can only be possibly explained through its microstructure. Figure 1 exhibits the Field Emission Scanning Electron Microscopy (FE-SEM) images of RS and BS at 1000X magnification. It may be noted that RS larger and more subangular particles, while the particles of BS are flakier. At the same time, it can be comprehended as well that RS offers more surficial contacts, while BS exhibits a dominance of edge contacts. Consequently, based on the contact interactions, RS is exhibiting a slightly higher magnitude of apparent cohesion. However, as can be noted from the magnitude of the shear strength parameters in Table 1, the two soils are not that vividly different from each other in the strength index.

Table 1. Geotechnical properties of RS and BS

Geotechnical Parameters	Red Soil (RS)	Black Soil (BS)
Specific Gravity	2.7	2.6
Atterberg Limit (%)		
Liquid Limit	45	95
Plastic Limit	19	30
Plasticity Index	26	65
Compaction Characteristics		
Maximum Dry Density (g/cc)	1.77	1.59
Optimum Moisture Content (%)	19.5	21.5
Grain Size Distribution (%)		
Sand	23.2	8.4
Silt	54.4	6.7
Clay	22.4	84.9
Soil Classification	ML	CH
Shear Strength Parameters		
Angle of internal friction (°)	17.53	13.0
Apparent cohesion (kPa)	12.4	6.1

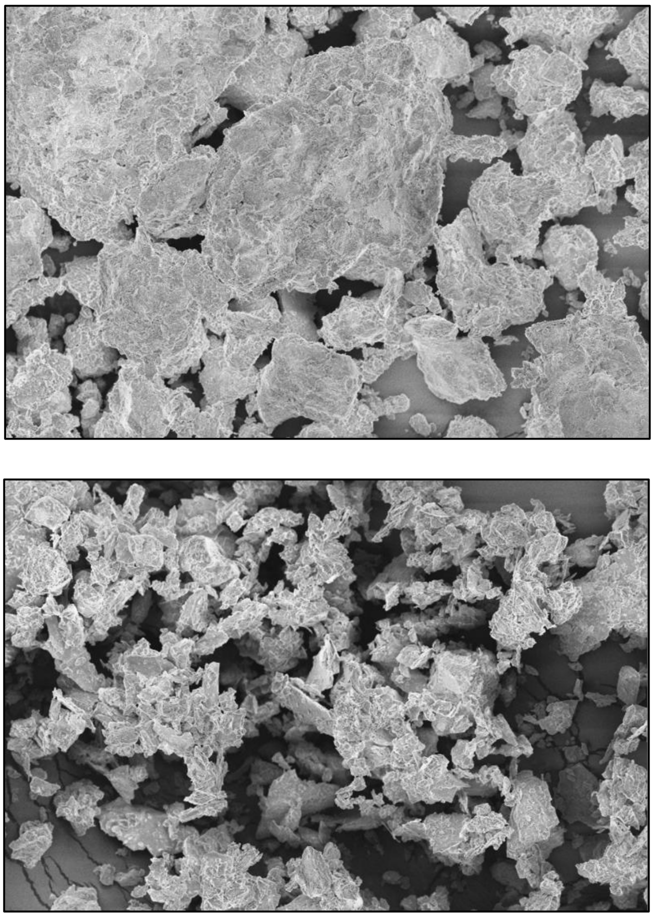

(a)

(b)

Figure 1. FE-SEM images at 1000X magnification (a) RS (b) BS

Several other laboratory tests were conducted to obtain input parameters required for reliable numerical modelling in the present study. These tests included the estimation of hydraulic conductivity at saturated and unsaturated states of the soils and several thermal properties of soil. Saturated hydraulic conductivity of the soils was determined using pre-fabricated cylindrical moulds whose dimensions were in accordance with the standards outlined in ASTM-D5856-15 [50]. The height and diameter of these moulds were 10 cm and 4.5 cm, respectively. For the permeability test, both RS and BS soil samples were compacted at their respective MDD and OMC. To ensure uniform distribution and flow of water through the soil samples, porous stones were placed at both the top and bottom of the sample in the mould. Furthermore, to prevent clogging of the porous stones with soil particles during testing, filter paper was placed along with the porous stones, with the filter paper being in direct contact with the soil. Prior to the use of porous stones in tests, they were examined for clogs and cleaned by boiling in water for 3-4 hours. The soil samples were fully saturated before starting the hydraulic conductivity tests using the falling head method. This method involved recording discharge readings over specific time intervals to accurately determine the hydraulic conductivity of both soil types. There are various techniques to identify the soil water characteristic curve, including both conventional and non-conventional methods [51]. For the present study, to determine the unsaturated hydraulic conductivity of both RS and BS soil specimens, the Hydraulic Conductivity Function (HCF) curve was derived from the Soil Water Characteristic Curve (SWCC). The data points for establishing the SWCC were obtained using a WP4-T Dew Point Potentiometer (Figure 2).

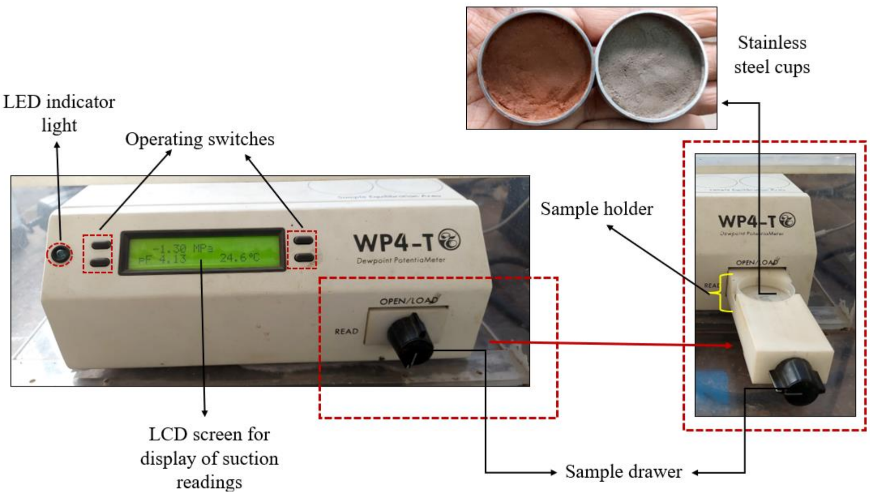

Figure 2. WP4-T Dewpoint Potentiometer with its operating parts, and the prepared soil sample in stainless steel cups

These data points consist of suction measurements at varying levels of water content in the soils. The working principle of WP4-T can be found in detail in ASTM-D 6836-02 Method D [52]. The obtained data points were fitted to the van Genuchten model [53] to obtain a smooth SWCC, and is represented in Figure 3(a). Equation 1 represents the van Genuchten formulation used for obtaining the SWCC. The curve fitting was performed by varying the parameters α, m, and n, which are known as the van Genuchten model parameters, and is expressed as

$$\theta = \theta_r + \frac{\theta_s - \theta_r}{[1+|\alpha h|^{n}]^{m}} \quad and \quad m = (1 - {}^{1}/_{n}) \qquad (1)$$

where θ represents the volumetric water content in soil (m^3/m^3), θ_r and θ_s represents the residual and saturated volumetric water content (m^3/m^3) of the soil, respectively.

The van Genuchten parameters were further utilized to derive HCF curves for RS and BS. Equation 2 represents the equation used for deriving the HCF curve. The HCF curves for both soils are depicted in Figure 3(b).

$$[K(h)] = \frac{K_s\{1-(\alpha h)^{mn}[1+(\alpha h)^n]^{-m}\}^2}{[1+(\alpha h)^n]^{ml}} \tag{2}$$

where K_s and $K(h)$ is the saturated and unsaturated hydraulic conductivity (m/s). Table 2 lists the hydraulic parameters of the RS and BS. It can be noted that the saturated permeability of the RS soil chosen for this study has a close agreement with the DL clay (ML soil classified as per USGS) reported by Rasool and Aziz [54].

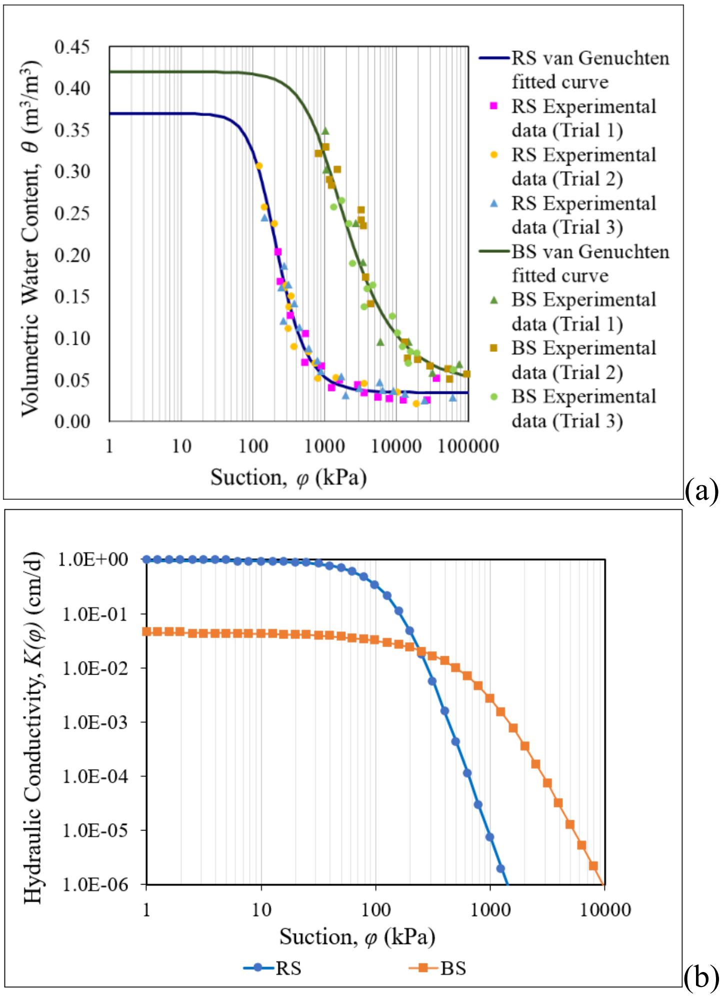

Figure 3. (a) Soil Water Characteristic Curve for RS and BS **(b)** Hydraulic Conductivity Function curve for RS and BS

Table 2. van Genuchten parameter, water content, permeability and shear strength parameters of RS and BS

Parameters	Red Soil (RS)	Black Soil (BS)
van Genuchten Parameters		
a (kPa)	167	1000
n	2.6	1.8
m	0.615	0.444
Water Contents		
Saturated Volumetric Water Content, θ_s (m^3/m^3)	0.42	0.37
Residual Volumetric Water Content, θ_r (m^3/m^3)	0.035	0.045
Saturated Permeability, K_s (m/s)	$1.10\text{x}10^{-7}$	$5.18\text{x}10^{-9}$

This study considers three different climatic conditions of RW, RW+SW and T(RW+SW). For T(RW+SW) case, temperature gradient along the depth of the soil is considered, which allows migration of water due to convection, as well as the freezing and thawing within the soil. An analysis that accounts for these mechanisms requires the use of the Soil Freezing Characteristic Curve (SFCC). The SFCC represents the relationship between unfrozen water content and negative temperatures. It is commonly assumed that at 0°C, liquid water freezes to ice. However, in reality, depending on the soil type, a depression in the freezing point of soil water occurs at negative temperatures due to adsorptive and capillary forces [55]. This results in a unique soil-water interaction for each soil, which is responsible for the existence of liquid water at temperatures below 0°C [56]. In the present study, the SFCC is obtained through an analytical expression proposed by Zhang *et al.* [57]. This approach combines the Clapeyron relationship (Equation 3) with the van Genuchten equation (Equation 1) to establish an equation for defining the SFCC (Equation 4). Thus, Equation 4 is used to calculate the variation in pore-water pressure of the unfrozen liquid water at sub-zero temperatures. Figure 4 displays the SFCC plotted for RS and BS using the aforementioned method.

$$\frac{\partial u_w}{\partial T} = \frac{h_{sf}}{v_w T_0} \tag{3}$$

where, ∂u_w represents the variation in water pressure within the unfrozen water in partially frozen soil, ∂T denotes the temperature change below the phase change temperature, h_{sf} is the latent heat of vapourization (334000 kJ/m^3), v_w represents the specific volume of water (1.0 L/kg), and T_0 corresponds to the standard freezing point of water at atmospheric pressure, which is considered as 0°C in this analysis.

The generated pore-water pressure from Equation 3 at the freezing point is then used to obtain the corresponding unfrozen volumetric water content as:

$$\theta_{uwc} = \theta_r + (\theta_s - \theta_r)\left[1 + \left(\alpha h_{sf} \ln \frac{T + 273.15}{T_0 + 273.15}\right)^n\right]^{-m} \tag{4}$$

where θ_{uwc} is the unfrozen water content in the soil.

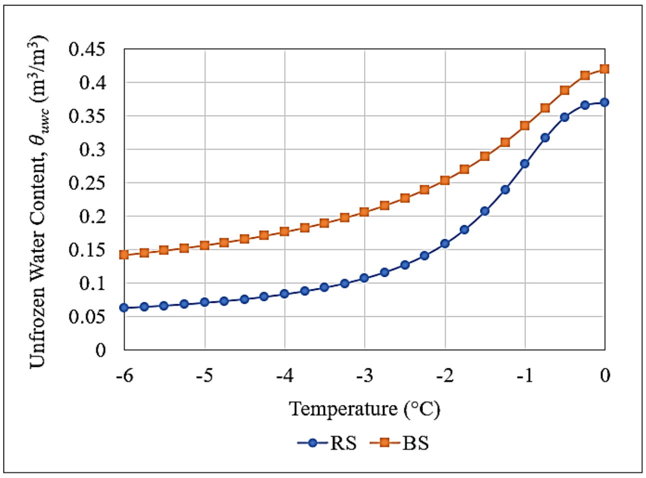

Figure 4. Soil Freezing Characteristic Curve for RS and BS

The thermal characteristics of both soils, RS and BS, in frozen and unfrozen states were determined using the KD2 Pro Thermal Properties Analyzer [58], developed by Decagon Devices (Pullman, Washington). The specifications followed by the KD2 Pro sensors adhere to ASTM D5334-14 [59]. The thermal properties of the RS and BS samples were determined on prepared soil samples in pre-fabricated cylindrical acrylic moulds by compacting the soil to maximum dry density and optimum moisture content. The height and diameter of this mould was 60 mm and 80 mm, respectively. These dimensions ensured that the recommended minimum distance between the sensor needle probe and the outer boundary of the acrylic cylindrical mould was not exceeded, thereby avoiding errors due to boundary effects from the heating of the sensor needle probe [60, 61]. In this study, the diameter of the mould was 5.86 times the needle diameter, which was sufficient to avoid any boundary effects. For measuring the thermal properties of the soil in frozen state, the prepared sample along with the mould was kept in deep freezer for 24 hours before taking the measurement with the help of these sensors. Figure 5 shows the ongoing measurement of thermal properties on the prepared sample using the KD2 Pro immediately after removing the sample from the deep freezer. For this study, the thermal conductivity and volumetric heat capacity were recorded at room temperature (unfrozen state) and at -10°C (frozen state), with the values listed in Table 3.

Table 3. Thermal parameters of RS and BS

Soil type	Unfrozen thermal conductivity (kJ/s/m/°C)	Frozen thermal conductivity (kJ/s/m/°C)	Unfrozen volumetric heat capacity (kJ/m^3/°C)	Frozen volumetric heat capacity (kJ/m^3/°C)
RS	0.001328	0.001873	3050	4633
BS	0.000989	0.001416	2862	3241

Figure 5. Measurement of thermal properties using KD2 Pro on prepared samples immediately after removal from the deep freezer

2.2 Methodology and Numerical Modelling

The present study is carried out on the terrain profile shown in Figure 6. The slope inclination angles (β) is varied are varied to 25°, 30°, 35°, 40°, and 45°. The maximum height of the considered terrain geometry is fixed at 20 m, with a 10 m fixed horizontal ground surface at the crest and a 5 m fixed vertical height at the toe sides of the sloping terrain. The dimensions of the terrain profile, particularly the height of the slope, are chosen based on the commonly adopted for stability analysis of hillslope as reported in earlier literature [62-66]. These studies typically consider slope heights ranging from 5-20 m, as it is commonly related to the prevalent height extents of the slope instability found in the regions. The vertical soil height to which water can infiltrate is considered as 4 m. This depth has been identified by several researchers as optimal for maximum infiltration, water storage, and moisture fluctuation [67-71]. This also means that the maximum depth of the critical slip surface for the failed soil mass cannot extend beyond this active depth.

The study considers two cases of homogeneous soil profiles and eight multi-couplets reconstituted varved clay profiles at each of the considered slope inclination angles. For all the slope profiles at all the different inclination angles, the analysis is carried out under three different climatic conditions – RW, RW+SW, and T (RW+SW). The climate variables used in the study include precipitation, air temperature, relative humidity, wind speed, solar radiation, and albedo. Table 4 provides the mean monthly magnitudes of the meteorological parameters as has been used in the present study.

For homogeneous soil terrain profiles, two slope profiles are created individually with RS and BS. In the analysis involving reconstituted varved clay in the same sloping terrain, RS and BS are arranged in alternate layers of the same total thickness (4 m) as considered for homogeneous soils. The reconstituted varved clay slope profile is considered in two types of sequential arrangements. In one set of laminae arrangements, BS occupies the topmost lamina, while in the other set, RS is the topmost lamina. The characteristics of slope failure, water infiltration, and runoff have been found to be different in both the cases of sequential arrangements. This indicates that the characteristics of the topmost lamina is important, as the land-climate interaction of the sloping terrain primarily occurs through that very lamina. The sloping terrain comprising reconstituted varved clay with BS as the topmost layer is designated as 2L_BS, 4L_BS, 8L_BS, and 16L_BS, where 'L' represents 'Lamina', and the numeric digits indicate the number of laminae. Similarly, for RS lying at the top, the reconstituted varved clays are represented as 2L_RS, 4L_RS, 8L_RS, and 16L_RS.

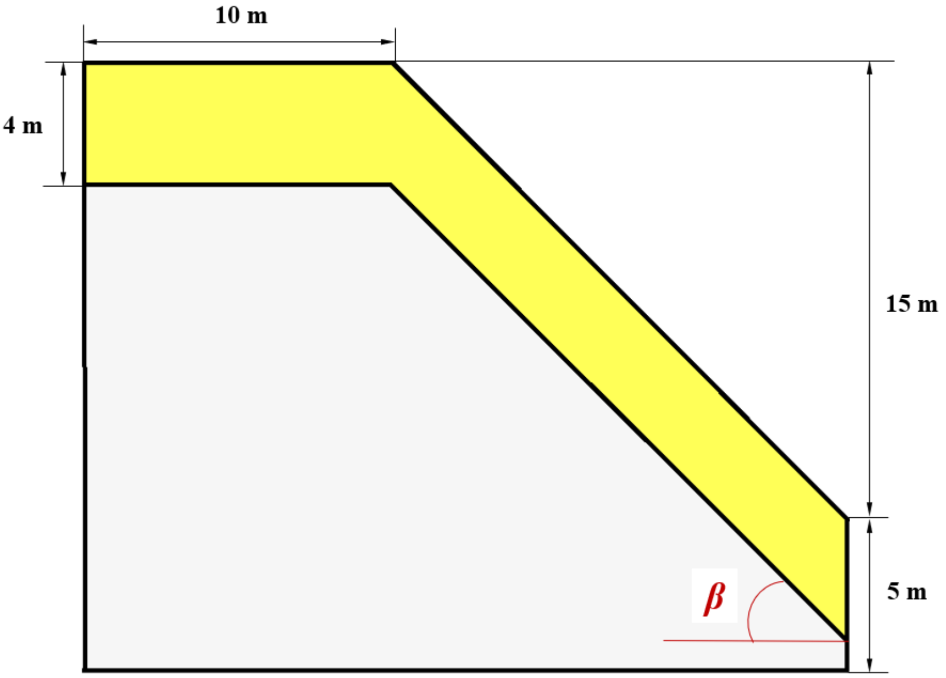

Figure 6. Schematic representation of a typical terrain profile

Table 4. Mean monthly meteorological data used in the study

Month	Average Precipitation (mm)	Average Temperature (°C)	Average Humidity	Average Wind Speed (m/sec)
January	29.5	-6.0	0.49	1.39
February	37.8	-4.0	0.52	1.39
March	71.3	-1.5	0.53	1.61
April	113.8	2.5	0.55	1.86
May	171.5	6.5	0.67	1.58
June	273.3	10.0	0.64	1.67
July	356.6	10.5	0.72	2.06
August	291.1	10.0	0.72	2.03
September	224.2	9.0	0.70	1.94
October	142.8	4.0	0.62	2.14
November	32.4	-0.5	0.55	1.83
December	24.2	-3.0	0.45	1.69

When numerical modeling is carried out without considering the thermal gradient across the soil depth, as in the cases of RW and RW+SW, the SEEP/W and SLOPE/W modules of GeoStudio are integrated. Whereas, when the temperature gradient is considered, which also leads to freezing and thawing, as in the case of T(RW+SW), the SEEP/W and TEMP/W modules of GeoStudio are coupled and then integrated with the SLOPE/W module. The coupling of the TEMP/W and SEEP/W modules accounts for the free convection of water induced by temperature changes. Free convection refers to the movement of water caused by temperature gradients [72]. Negative temperatures lead to the freezing of water in soil pores, while thawing occurs as the temperature turns positive. This phase change of water in soil pores is considered in the analysis by varying the density of water with temperature according to Thiesen's formula [73], as shown in Figure 7.

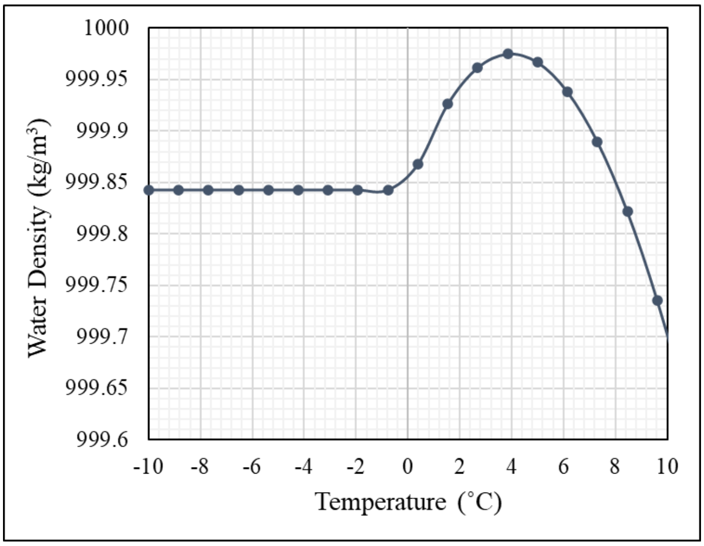

Figure 7. Water density function as defined by Thiesen formulation

2.2.1 Land-Climate-Interaction (LCI) Boundary Conditions

In cold region geotechnical engineering studies that address the impact of climate change, for Himalayan and sub-Himalayan regions as well, it is crucial to consider the interactions between various climatic components with the ground [74,75]. Understanding these interactions is essential for assessing how geo-structures behave in cold regions. This study, therefore, incorporates LCI boundary conditions, which account for the interaction of different climatic variables such as air temperature, precipitation, relative humidity, wind speed, solar radiation, and albedo with the ground profile [76]. These climatic variables also influence water dynamics along the depth of the soil during freezing and thawing as discussed above.

The present study utilizes ten years of average real-time meteorological data obtained from an online climate data collector [77]. Each set meteorological data is averaged over a month. Months with an average temperature of 0°C or below are considered winter months (November to March), while those with a positive average air temperature are considered summer months (April to October). The analysis begins in November, marking the onset of the winter season during which precipitation occurs as snow (days 0 to 151). Consequently, whenever there is snowfall, snow accumulates on the ground surface. Day 152 marks the start of April and the beginning of the summer season during which precipitation occurs as rainfall. During this summer season, the infiltration of water from precipitation and snowmelt occurs and influences slope stability, with part of the water contributing to runoff. Additionally, it is assumed that the soil has an initial suction of -1500 kPa for all ten slope profiles.

In areas with snow, albedo is a crucial consideration as it governs the rate of snow melting. Albedo (α) varies from 0.9 for freshly fallen snow to about 0.2 for dirty snow, and during melting, the albedo is around 0.4 [78]. In this study, an albedo of 0.9 is considered for the winter season and an albedo of 0.4 is used for the summer months when snow is melting.

In this study, the net solar radiation is estimated based on the specific day of the year and the latitude of the study area. The latitude of the study area is 27.85°. The net solar radiation, q_{ns}, is estimated as follows:

$$q_{ns} = (1-\alpha)q_s \tag{5}$$

where, q_s is the shortwave radiation and is calculated as:

$$q_s = (a_s + b_s \frac{n}{N})q_{ext} \tag{6}$$

Here, a_s and b_s are regression constants and are assumed to be 0.25 and 0.5, respectively, based on recommendations by Allen *et al.* [79], n is the actual duration of sunlight, N is the maximum possible duration of sunlight, and q_{ext} is the extraterrestrial radiation. In this study, $\frac{n}{N}$ is considered equal to 1 for simplification, implying a clear sky (i.e. no clouds).

The extraterrestrial radiation q_{ext} is calculated as follows:

$$q_{ext} = \frac{1}{\pi} G_{sc} d_r [w_s \sin\varphi \sin\delta + \cos\varphi \cos\delta \sin w_s] \tag{7}$$

where, G_{sc} is the solar constant with a value of 118 MJ/m^2/day, d_r represents the inverse of the relative distance between the Earth and the Sun (in m), w_s is the sunset hour angle, φ^L denotes the latitude of the study area, which is 27.85° in this study. Finally, δ is the solar declination, which is given by equation:

$$\delta = 0.409 \sin(\frac{2\pi}{365} J - 1.39) \tag{8}$$

where J is the day of the year (e.g., January 1 is day 1). Furthermore, the sunset hour angle ω_s is given by:

$$\omega_s = \cos^{-1}(-\tan\varphi^L \tan\delta) \tag{9}$$

After the winter season, when the temperatures rise above 0°C during summers, the accumulated winter snow begins to melt. The converted water from snow is referred to as Snow Water Equivalent (SWE) and represents the water stored in a snowpack. SWE not only affects the infiltration and runoff characteristics over the slopes but also affects their stability, as the additional water from snowmelt influences the pore water pressure distribution in soil slopes. SWE at the current numerical time step (SWE_t) (mm/day) is calculated using Equation 10.

$$SWE_t = SWE_{t-1} + SF - SM \tag{10}$$

where SWE_{t-1} is the snow water equivalent at the previous numerical time step (mm/day), SF is the snowfall precipitation rate and SM is the snowmelt rate (mm/day).

The snowmelt rate in the present study is calculated using Equation 11, as proposed by the U.S. Army Corps of Engineers [80]. This equation utilizes an energy balance approach to determine the rate of snow melting. It is important to note that there are two separate equations available to calculate the rate of snow melting, one for rainy days and one for non-rainy days. In the present study, the equation for rainy days is used since the analysis considers the average precipitation throughout the given month. Therefore, Equation 11 is applied to calculate the rate of snowmelt in this study.

$$SM = C[0.09 + (0.029 + 0.00504v + 0.007P)(T_a - T_F)] \tag{11}$$

where v is the wind speed (miles/hour), T_a is the air temperature (°F), T_F is the freezing temperature (°F) which is considered as 32°F in the present study, and C is the coefficient to account for variations which is arbitrarily assumed as 2.5 in the present study. This choice of C is based on several factors, including the non-linear and diverse nature of snowmelt-related variables. This value of 2.5 is supported by findings from various studies [81-84], which collectively demonstrate the substantial variability in snowmelt processes and their significant impact on hydrological responses.

As stated above, the Snowfall (SF) precipitation is calculated based on given temperature during the particular time which is represented numerically as given in Equation 12.

$$SF = Q_p \times P \tag{12}$$

where P is the precipitation (mm/day), and Q_p is the thermal factor given in Equation 13.

$$Q_p = 0\ (if\ T_a > T_f);\ Q_p = 1\ (if\ T_a < T_f) \tag{13}$$

2.2.2 Slope Stability and Shear Strength of Soil under Unsaturated Conditions

The LCI boundary condition is applied at the ground level (top surface) for all three considered climate scenarios, which simulates the dynamic interactions between the land surface and atmospheric conditions (as discussed in detail in Section 2.2.1). This boundary condition ensures that the stress states induced by environmental factors, particularly changes in stresses due to water infiltration into the soil slope, are accurately reflected in the SEEP/W module at each time step. These stresses are then utilized by the SLOPE/W module to compute the Factor of Safety (FoS), integrating both hydraulic and mechanical behaviors to provide a comprehensive view of slope stability.

In the present study, the slope stability analysis employs the Mohr-Coulomb material model in an unsaturated state. This particular model, which was proposed by Vanapalli *et al.* [85], is based on Bishop's effective stress principle, and is described using Equation 14.

$$\tau = c' + (\sigma_n - u_a)tan\phi' + (u_a - u_w)[\chi tan\phi'] \tag{14}$$

where τ is shear strength of soil (kPa), σ_n is net total stress (kPa), u_a is pore air pressure (kPa), c' is effective cohesion (kPa), ϕ' is effective angle of internal friction (°) and χ is parameter related to the degree of saturation, which is defined by Vanapalli *et al.* [85] as:

$$\chi = \frac{\theta_w - \theta_r}{\theta_s - \theta_r} \quad (15)$$

The slope stability analysis is performed using the limit equilibrium technique proposed by Morgenstern and Price [86]. This method employs FoS equations with respect to the moment equilibrium (FoS_m) and with respect to force equilibrium (FoS_f), as provided in Equation 16 and Equation 17, respectively.

$$FoS_m = \frac{\sum[c'lR + \{N - u_w l\chi - u_a l(1-\chi)\}Rtan\phi']}{\sum Wx - \sum Nf \pm \sum Dd \pm \sum Aa} \quad (16)$$

$$FoS_f = \frac{\sum[c'lcos\alpha + \{N - u_w l\chi - u_a l(1-\chi)\}tan\phi' cos\alpha]}{\sum Nsin\alpha - \sum Dcos\omega \pm \sum A} \quad (17)$$

where W is total weight of a slice of width b and height h, N is total normal force on the base of the slice, D is external point load, R is radius of a circular slip surface or moment associated with the mobilized shear force, x is horizontal distance from the centreline of each slice to the centre of rotation or to the centre of moments, d is perpendicular distance from a point load to the centre of rotation or to the centre of moments, a is perpendicular distance from the resultant external water force to the centre of rotation or to the centre of moments, A is resultant external water forces, ω is angle of the point load from the horizontal, α is angle between the tangent to the centre of the base of each slice and the horizontal, and l is base length of each slice.

In this study, the mobilized shear and normal stresses in unsaturated states are determined using Equation 18 and Equation 19, as proposed by Fredlund and Krahn [87].

$$\tau_m = \frac{l}{F}(c' + (\sigma_n - u_a)tan\phi' + (u_a - u_w)tan\phi^b \quad (18)$$

$$N = \frac{W + (X_R - X_L) - [\frac{c' + lsin\alpha + u_a bsin\alpha\left(tan\phi' - tan\phi^b\right) + u_w lsin\alpha tan\phi^b}{F}}{cos\alpha + \frac{sin\alpha tan\phi'}{F}} \quad (19)$$

where τ_m is shear force mobilized on the base of each slice and F is horizontal interslice normal forces. The subscripts L and R designate the left and right sides of the slice, respectively.

In this study, the inclination angle of slopes and the change in pore-water pressure due to water infiltration are the driving forces, whereas the shear force generated along the slip surface acts as the resisting force. In slope stability analysis, when the FoS drops below 1, the slope becomes unstable and eventually fails. An FoS equal to 1 signifies that the resisting forces are just insufficient to counteract the driving forces which marks the onset of slope instability. This condition indicates imminent stability under ideal circumstances without considering uncertainties. However, in reality, significant uncertainties are associated with shear strengths around the failure plane due to several external factors. Consequently, under static conditions, an FoS of 1.5 [88] is commonly adopted during stability analysis to ensure a safety margin for slopes.

In the present study, the slip surface assessment for homogeneous sloping terrain profiles is determined by the entry-exit method, while the block specified method is used for reconstituted varved clay slope profiles. The block specified method of search technique is best suited when there is a low-strength layer in the slope profile, and the sloping segment of the terrain is significantly longer than the ground projection at both ends. In the case of slopes consisting of varved clays, RS and BS are arranged alternately in different numbers of layers, as mentioned above. However, in these layered structures, BS has lower shear strength parameters compared to RS (Table 1). Therefore, the block specified method is used for the stability assessment of layered soil slope profiles. For the reconstituted varved clay slope profiles, the vertical lines in both the upper and lower grids are maintained at 5, while the number of inclined lines parallel to the slope is determined by the number of laminae constituting the slope profile. If N is the number of layers, then the number of grid lines in the horizontal direction is taken as N+1. This ensures that the horizontal grid line lies at the top most (ground surface) and bottom most of the sloping profiles and at each interface of RS and BS. Therefore, the number of horizontal lines in both left and right grids is 3, 5, 9, and 17 for 2-layered, 4-layered, 8-layered, and 16-layered reconstituted varved clay slope profiles, respectively. For homogeneous soil slope cases where the entry-exit method is used, 12 entry and exit points are employed. Figure 8(a) shows a typical example of the entry-exit method applied to a homogeneous BS slope profile (a similar one would be used for RS profile as well), while Figure 8(b) illustrates the use of the block specified method in a reconstituted varved clay slope with multiple laminae.

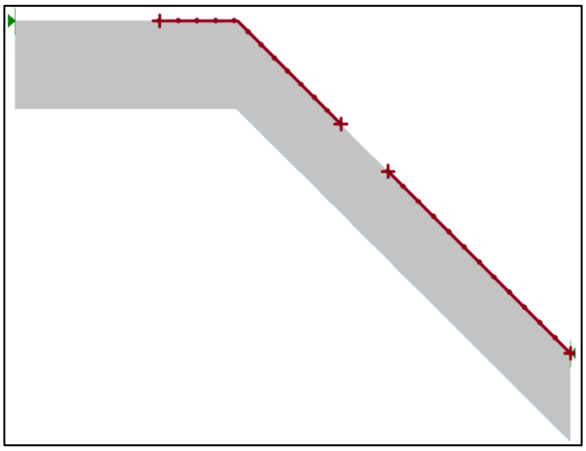

Figure 8(a). Typical representation of entry-exit method of slip surface assignment for slopes with homogeneous material profiles

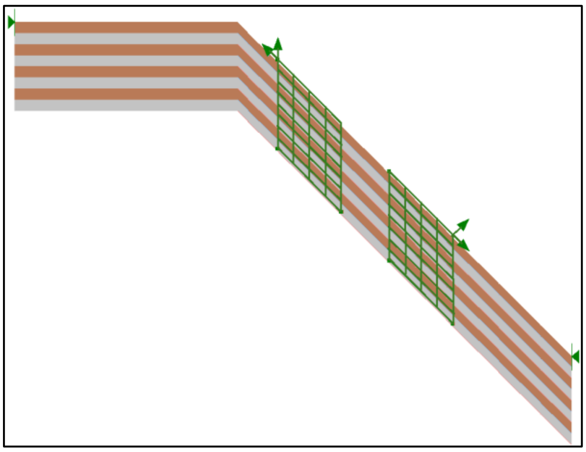

Figure 8(b). Typical representation of block -specified method of slip surface assignment for slopes profile with multi-couplet laminae

3. Results and Discussions

This section discusses the results obtained from the study at different combinations of three climatic conditions [RW, RW+SW, and T(RW+SW)], five slope inclination angles (25°, 30°, 35°, 40°, and 45°), and ten slope profiles (RS, BS, 2L_BS, 4L_BS, 8L_BS, 16L_BS, 2L_RS, 4L_RS, 8L_RS, 16L_RS). The section is further subdivided to discuss how these variables affect the FoS (Section 3.1) and water dynamics (Section 3.2) in various considered slope profiles.

Two important points should be noted for this study. Firstly, although the study period spans 365 days, many graphical plots represent the data for a restricted time period because the magnitudes remain constant outside these time periods. Secondly, it is not feasible to present all the graphs and figures from every analysis conducted in this study; therefore, only selected graphs and figures are used to convey the findings. The complete details of the results are communicated with the help of tables (Table 5 to Table 8).

3.1 Analysis of Slope Instability in Different Soil Profiles for RW, RW+SW, and T(RW+SW) Scenarios

This section discusses the transient FoS trends for all ten considered soil profiles under three different climate conditions of RW, RW+SW and T(RW+SW) at different slope inclination angles. Additionally, the day at which slope fails (FoS < 1.5) is examined and the area of the failed soil slope mass is analyzed for different soil slope profiles at different inclination angles.

Figure 9 shows the variation of the FoS over the period of 0 to 220 days for various climatic conditions and selected slope profiles for slope inclination angle of 30°. Figures 9(b), 9(d), 9(f), and 9(h) illustrate the FoS vs. time plots for the slope profiles of RS, BS, 2L_BS, and 2L_RS under the T(RW+SW) climatic condition, while Figures 9(a), 9(c), 9(e), and 9(g) show the FoS vs. time plots for these slope profiles under the RW and RW+SW climatic conditions, plotted together. The FoS vs. time graph for the T(RW+SW) condition is represented separately to clearly show the increased magnitude of FoS during the winter season (0 to 151 days). During this period, precipitation occurs as snowfall, which does not influence water dynamics in and around the soil in case of RW and RW+SW climatic conditions. However, in case of T(RW+SW), the atmospheric temperature affects the ground surface temperature of the terrain, which influences the temperature gradient across the soil depth. When the atmospheric temperature drops below 0°C during the winter months, water from various depths in the soil is drawn towards the ground surface due to free convection (as discussed in detail in Section 2.2). Water migrates to the ground freezing front and simultaneously freezes, which leads to an increase in FoS during the winter season, as evident from Figures 9(b), 9(d), 9(f), and 9(h). This increase in FoS of slopes during winter due to the freezing of water in the soil influences its failure during the thawing period. In the succeeding paragraph, it is discussed how the increased FoS during winter due to soil freezing affects the timing of slope failure as the water thaws in summer, and under what conditions this occurs. Under normal conditions, when the ground temperature is not considered, such as in the cases of RW and RW+SW, the FoS remains unchanged and constant throughout the winter season, as demonstrated by Figures 9(a), 9(c), 9(e), and 9(g).

It is observed that in the RS and 2L_RS slope profiles, the rise in FoS is quite sharp before attaining a constant FoS magnitude (Figures 9b and 9h) compared to BS and 2L_BS (Figures 9d and 9f). In BS and 2L_BS, the increase in FoS due to freezing soil is gradual before it attains a constant value during the winter season. In the case of slopes constituted by BS and 2L_BS, the interaction of the ground surface with the regional climate occurs through BS, which acts as the freezing front. Similarly, for slopes constituted by RS and 2L_RS, the interaction occurs through RS, where RS serves as the freezing front. These trends in FoS over time for slopes with different ground surface soil under negative temperatures can be attributed to differences in the thermal properties and soil freezing characteristics of RS and BS (Table 3 and Figure 4). Due to the higher thermal conductivity and heat capacity of RS, it has higher efficiency to transfer and store thermal energy (Table 3). When exposed to negative temperatures, RS loses heat rapidly, which results in a quick reduction in temperature and rapid formation of ice from water within its pores. Moreover, the SFCC (Figure 4) indicates that RS can retain a lesser volume of unfrozen water compared to BS at the same freezing temperature, which further accelerates the freezing of water in RS. Therefore, when water in RS changes from liquid to solid, there is a sharper rise in FoS in homogeneous RS and 2L_RS slopes compared to homogeneous BS and 2L_BS slopes. The same trend of a sharp increase in FoS observed for RS and 2L_RS is noted for other slope profiles with RS as the topmost lamina, such as 4L_RS, 8L_RS, and 16L_RS, compared to slopes with BS as the topmost lamina, like 4L_BS, 8L_BS, and 16L_BS. When the summer season begins and atmospheric temperatures become positive, the frozen water in the soil starts to melt. The positive temperature will gradually migrate from the surface to the entire depth of the soil slope, causing melting to begin at the ground surface and progress downward. Among soil profiles with RS and BS as the topmost lamina, due to the higher thermal conductivity and heat capacity of RS, the frozen water in RS will melt more rapidly than in BS during thawing. Rapid melting of frozen water in soil, combined with water already infiltrating from melting of snow and rainfall, leads to earlier slope failure in slopes with RS as the ground surface under T(RW+SW) climatic conditions compared to the RW+SW case (Figure 9 and Table 5). However, for slope profiles with BS as the ground surface (or topmost lamina), melting is slower due to the thermal properties of BS. As a result, slope failure occurs later under T(RW+SW) conditions than under RW+SW conditions (Figure 9 and Table 5). These observations hold true for all other slope profiles with different inclination angles considered in this study. The above findings indicate that although freezing of water inside soil slopes increases the FoS magnitude, its failure during the thawing period is influenced by the thermal properties of the soil constituting the ground surface.

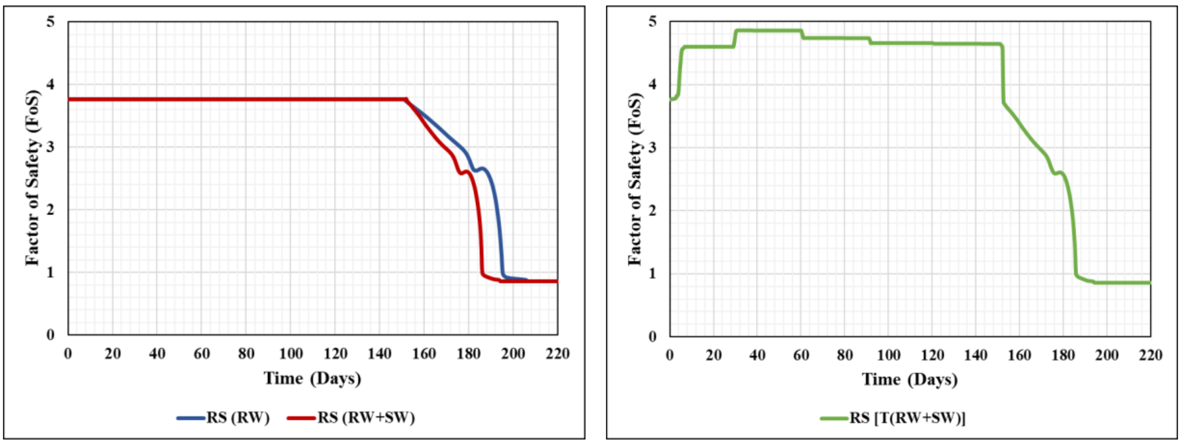

(a) (b)

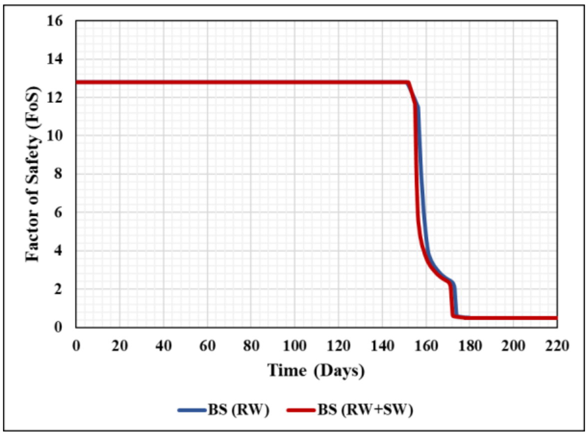

(c)

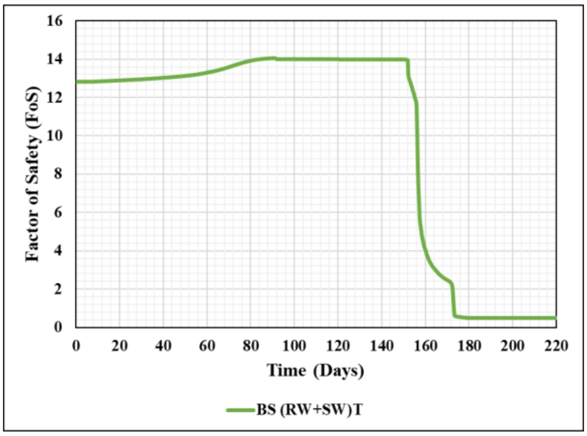

(d)

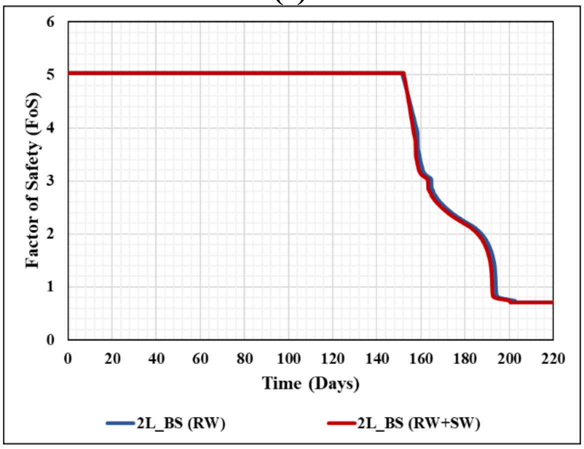

(e)

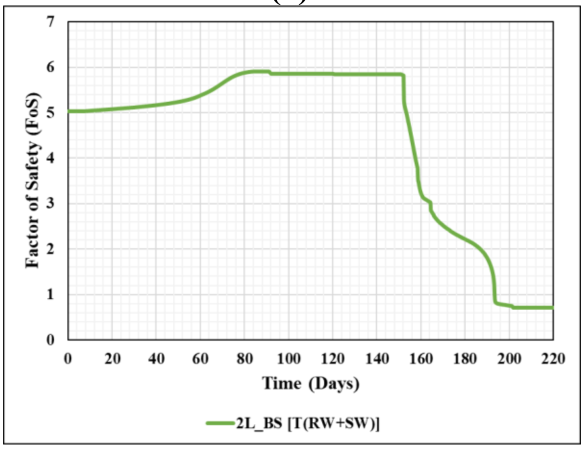

(f)

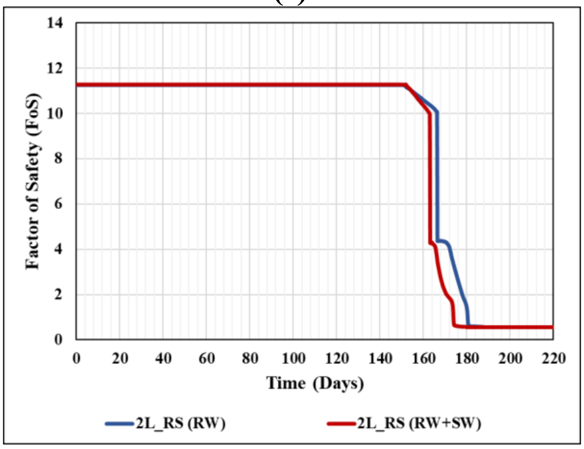

(g)

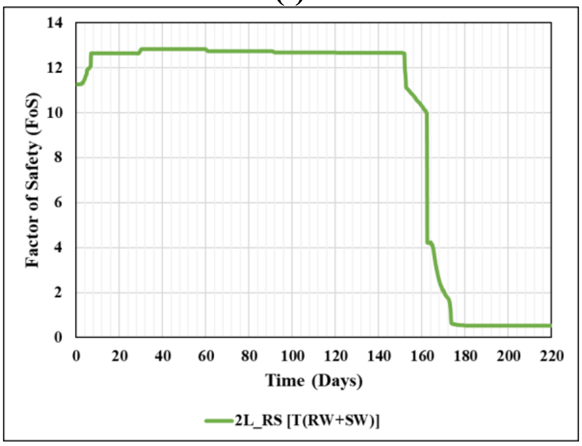

(h)

Figure 9. Temporal variation of FoS in various slope profiles with 30° inclination and subjected to varied climatic conditions: **(a)** RS under RW and RW+SW **(b)** RS under T(RW+SW) **(c)** BS under RW and RW+SW **(d)** BS under T(RW+SW) **(e)** 2L_BS under RW and RW+SW **(f)** 2L_BS under T(RW+SW) **(g)** 2L_RS under RW and RW+SW **(h)** 2L_RS under T(RW+SW)

The increase in the pore water pressure in the soil receives contribution from rain, melting snow on the ground and melting ice within the frozen soil. This increased pore water pressure reduces the shear strength of the soil and, consequently, the FoS, as shown in Figure 10. The figure presents the FoS versus time plots for all 10 slope profiles considered at a slope inclination angle of 30° during the summer season. Figures 10(a) and 10(b) illustrate the FoS variation with time for homogeneous slopes of RS and BS, respectively. Figures 10(c), 10(e), 10(g), and 10(i) depict the FoS trends over time for 2L_BS, 4L_BS, 8L_BS, and 16L_BS respectively, while Figures 10(d), 10(f), 10(h), and 10(j) present these trends for 2L_RS, 4L_RS, 8L_RS, and 16L_RS respectively. It can be observed from Figure 10 that different soil profiles exhibit unique responses in the variation of FoS due to infiltrating water under different climatic conditions. Additionally, these figures indicate that the consideration of additional water from snowmelt in the RW+SW and T(RW+SW) cases has a more significant impact on the homogeneous RS slope profile and reconstituted varved slope profiles with RS as the topmost layer compared to slopes consisting of homogeneous BS and reconstituted varved slopes with BS as the topmost lamina. This is evident from the greater difference in FoS magnitudes between the RW+SW and T(RW+SW) conditions compared to RW for the same corresponding times. This indicates that slope profiles with topmost layer as RS are more sensitive to additional water from snowmelt. These observations are linked to the time taken to reach maximum cumulative net infiltration in the reconstituted varved clays with two arrangements and are discussed in detail in the succeeding section, Section 3.2.

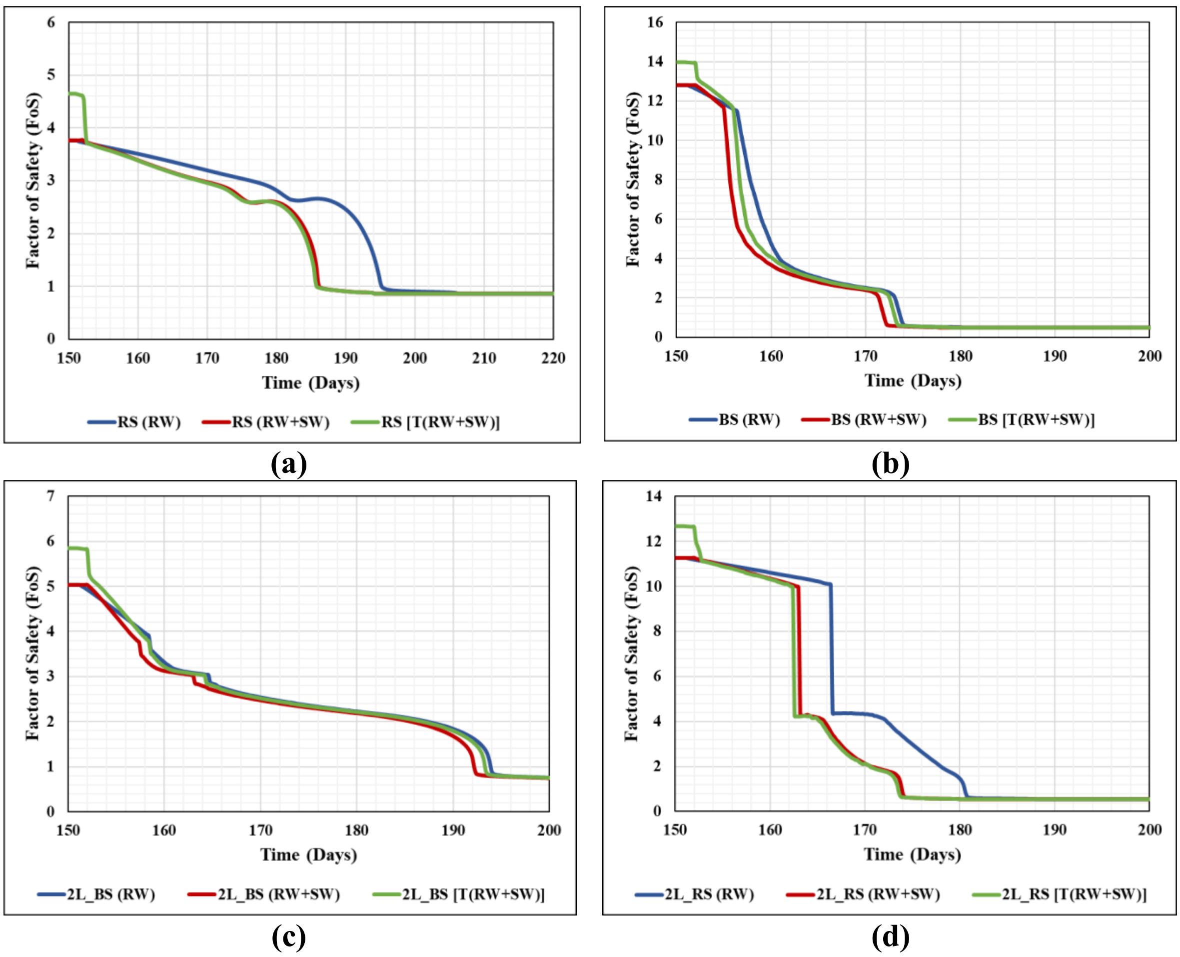

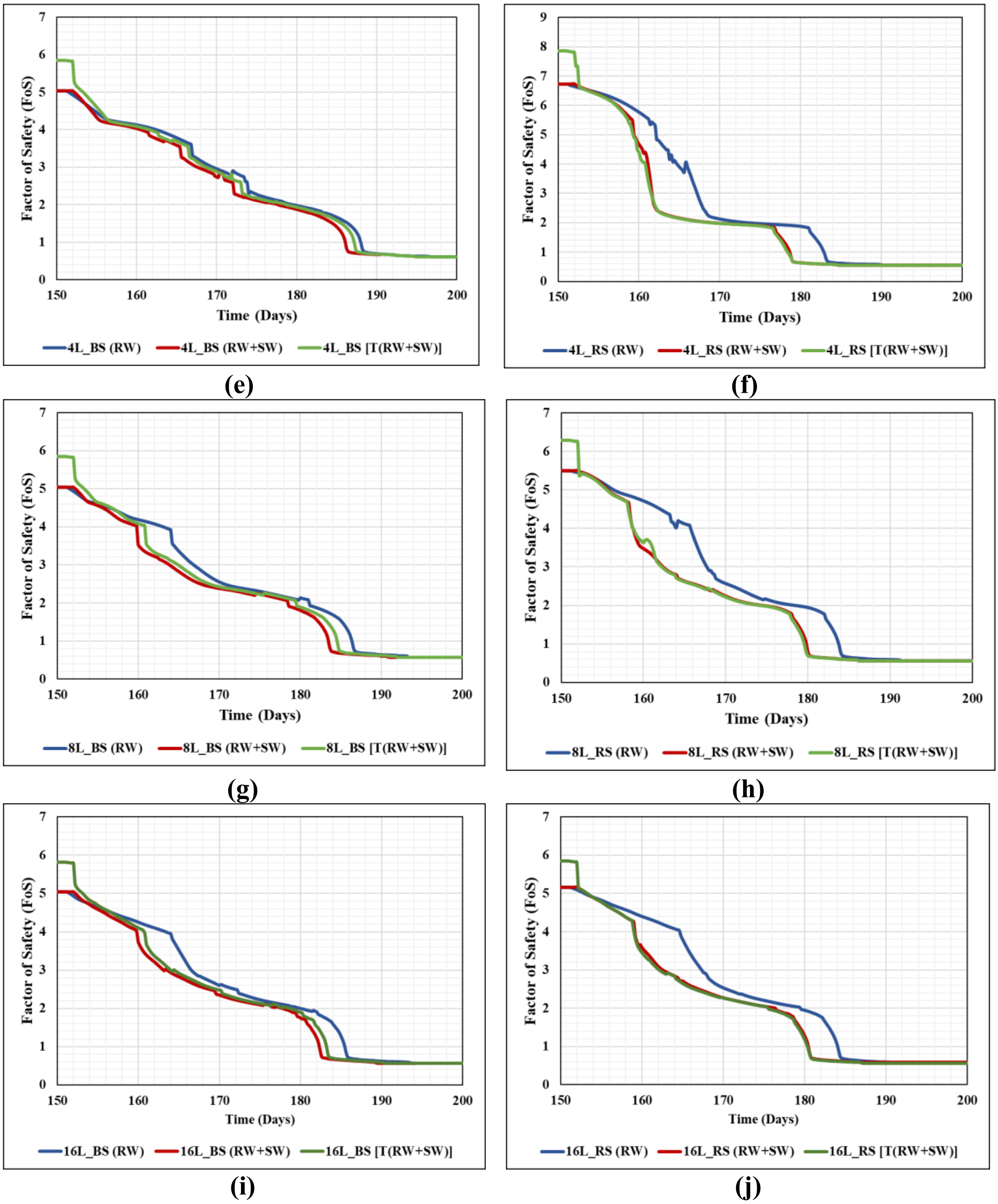

Figure 10. Temporal variation in FoS in slope profiles with 30° slope inclination for RW, RW+SW and T(RW+SW) scenarios **(a)** RS **(b)** BS **(c)** 2L_BS **(d)** 2L_RS **(e)** 4L_BS **(f)** 4L_RS **(g)** 8L_BS **(h)** 8L_RS **(i)** 16L_BS **(j)** 16L_RS

Further, from Figures 10(a) and 10(b), it is observed that among homogenous RS and homogenous BS slopes, the rate of decrease in FoS during the summer season is much more rapid in the case of homogeneous BS slope profiles as compared to homogenous RS slope profiles for all the considered climatic conditions of RW, RW+SW, and T(RW+SW). Due to this, slope failure occurs earlier in slopes consisting of BS than in those with RS. It is interesting to note that this behavior is observed even though the FoS before the beginning of the summer season for the homogeneous BS slope profile is significantly higher than for the homogeneous RS slope profile. The initially high FoS of the BS slope profile can be attributed to its higher χ parameter, which results from a greater difference in saturated volumetric water content (θ_s) and residual volumetric water content (θ_r), which significantly influences the shear strength of the soil (Equation 18). The values of θ_r and θ_s for both RS and BS are listed in Table 2. The initial applied suction of -1500 kPa in all soil slopes is higher than the air entry value (a) of both RS and BS (Figure 3a and Table 2). The rapid decrease in FoS for the homogenous BS slope profile is attributed to the high rate of water infiltration due to the higher hydraulic conductivity of BS compared to RS at the high applied suction magnitude. From the HCF curve in Figure 3(b), it is evident that although the saturated hydraulic conductivity of RS is greater than that of BS when the soils are fully saturated, BS exhibits higher hydraulic conductivity than RS beyond the intersection of their HCF curves. This intersection point is referred to as the 'breakthrough suction point' [89, 90]. Therefore, as the hydraulic conductivity of BS is higher for the considered initial suction in the slope profile, water infiltrates more rapidly in homogenous BS slopes compared to homogenous RS slopes. This leads to earlier attainment of saturation in slopes constituting of BS, which cause them to fail earlier than slopes consisting of RS.

Figures 10(c) to 10(j) indicate that all reconstituted varved clay slopes fail earlier when the topmost lamina is RS, under all considered climatic conditions, compared to when the topmost lamina is BS. This can be linked to the phenomenon known as 'breakthrough.' Breakthrough occurs when the 'breakthrough suction point' is reached in the layered soils and happens when water infiltrates from a finer soil layer into a coarser soil layer. [91]. In the present study, laboratory tests show that BS is finer than RS (Table 1 and Table 2). When such soil layering exists, the finer-grained layer retains water at the interface, restricting water flow into the coarser-grained layer. For instance, in two-layered reconstituted varved slopes, when BS forms the uppermost layer of the reconstituted varved slopes (2L_BS), water infiltrating from BS to RS is hindered at the interface due to the contrasting hydraulic characteristics between the two soils at the BS-RS interface. This results in delayed water infiltration into the lower RS layer, which leads to delayed attainment of maximum cumulative net infiltration and, consequently, slope failure when BS overlies RS. While in the case of two-layered reconstituted varved clays with RS forming the uppermost lamina, water infiltrates from RS to BS, and no such hindrance is observed. The restriction of infiltration of water in reconstituted varved clay slopes with BS as the topmost lamina results in a delayed failure compared to reconstituted varved clay slopes with RS as the topmost lamina for the same number of laminae. This observation is valid for all climatic conditions of RW, RW+SW, and T(RW+SW), and for different slope inclination angles. However, for different slope inclination angles, the time of slope failure and the extent of the failed soil area vary with each slope inclination angle, as discussed in subsequent section. The durations required for the initiation of failure in the reconstituted varved clay slope profiles (with different sequential arrangements) are listed in Table 5. Further, the variation in the time of failure for slopes comprising reconstituted varved clays in the two sequential arrangements is linked to the time taken to reach maximum cumulative net infiltration in these arrangements, as discussed in detail in Section 3.2 of the paper.

It is further observed from Figure 10 that for homogeneous RS slopes (Figure 10a) and reconstituted varved slopes with RS as the topmost lamina (Figures 10d, 10f, 10h and 10j), the curves for RW and RW+SW appear to overlap. In contrast, for homogeneous BS slopes (Figure 10b) and reconstituted varved slopes with BS as the topmost lamina (Figures 10c, 10e, 10g and 10i), the curves are close but do not overlap. Therefore, accurately determining the time of slope failure from visual identification from these graphs alone is challenging. Alternatively, the failure times for various slope combinations have been listed in Table 5. It is observed that as the slope inclination angle increases, the slope fails early for a given profile under all climatic conditions. For example, in the RW case, the RS slope profile fails at days 196.2, 194.4, 193.4, 192.6, and 191.6 for inclination angles of 25°, 30°, 35°, 40°, and 45°, respectively. Similar trends of early slope failure with increased slope inclination angle is observed for all other slope profiles under different climatic conditions.

Table 5 also indicates that slope failure occurs earliest in homogeneous BS slopes among all considered profiles, for all the of slope inclination angles. For instance, under RW climatic conditions, homogeneous BS slopes fail at 174.8, 173.4, 172.2, 171, and 169.8 days for inclination angles of 25°, 30°, 35°, 40°, and 45°, respectively, while all other slope profiles fail later. This trend is consistent under RW+SW and T(RW+SW) climate conditions as well. The early slope failure in BS can be attributed to its lower shear strength properties compared to RS. As shown in Table 1, both cohesion and internal angle of friction for BS are lower than those for RS, resulting in lower shear strength and making BS more susceptible to slope failure during water infiltration. The maximum time to slope failure is observed in homogeneous RS slopes under RW climatic conditions. However, under RW+SW and T(RW+SW) conditions, the maximum time to slope failure occurs in 2L_BS slopes for all slope inclination angles. Additionally, the number of laminae and the lamina constituting the ground surface influence the time to slope failure. Although homogeneous BS slopes fail earliest at all slope inclination angle and all climatic conditions, reconstituted varved slopes with BS as the topmost lamina fail later compared to the slope profiles with RS as the topmost lamina for the same number of laminae. For example, under RW climatic conditions and a slope inclination angle of 25°, the failure times for 2L_BS, 4L_BS, 8L_BS, and 16L_BS slopes are 195.2, 189.4, 187.6, and 186.6 days, respectively, while for 2L_RS, 4L_RS, 8L_RS, and 16L_RS slopes, the failure times are 180.8, 183.4, 184.4, and 184.8 days, respectively. This delay in slope failure when BS is the topmost lamina is consistent across all slope inclination angles and climatic conditions. The delayed failure in reconstituted varved clays with BS as the topmost lamina can be attributed to the water retention mechanism of BS when it overlies RS as discussed above. In a 2-layered varved slope, a water-retaining interface forms once in the 2L_BS slope, while in the 2L_RS slope, no such interface is formed and water simply infiltrates from RS to BS. For slopes with 4, 8, and 16 layers, the water-retaining interface occurs in 2, 4, and 8 numbers, respectively, when BS occupies the topmost lamina; while it occurs for 1, 3, and 7 numbers, respectively, when RS is the topmost lamina. The number of water-retaining interface formed in the multi-couplet depends on the number of BS-RS interfaces hindering the free diffusion of water from a higher permeable medium to a lower one. Since the BS-RS interface is more prevalent in slopes with BS as the topmost lamina compared to those with RS, the time to failure is earlier in reconstituted varved slopes with RS as the topmost lamina compared to those with BS as the topmost lamina, for the same number of laminae. This observation holds true for all climatic conditions and slope inclination angles.

Table 5. Duration (in days) until FoS drops below 1.5 under different climatic conditions

Water from Rain only [RW]						
Soil Slope		**Slope Inclination Angle**				
		25°	**30°**	**35°**	**40°**	**45°**
Homogenous	**RS**	196.2	194.4	193.4	192.6	191.6
	BS	174.8	173.4	172.2	171.0	169.8
Reconstituted Varved Clay	**2L_BS**	195.2	193.0	189.0	185.0	181.4
	4L_BS	189.4	186.6	183.4	180.6	178.4
	8L_BS	187.6	185.2	182.2	180.4	178.4
	16L_BS	186.6	184.4	182.4	180.0	178.4
	2L_RS	180.8	180.0	179.4	179.2	179.0
	4L_RS	183.4	181.8	180.4	179.2	178.6
	8L_RS	184.4	182.8	181.0	179.6	178.4
	16L_RS	184.8	183.2	181.4	179.6	178.2
Water from both Rain and Snowmelt [RW+SW]						
Soil Slope		**Slope Inclination Angle**				
		25°	**30°**	**35°**	**40°**	**45°**
Homogenous	**RS**	187.6	185.8	183.6	181.6	179.6
	BS	173.2	171.8	170.2	168.6	167.0
Reconstituted Varved Clay	**2L_BS**	194.8	191.2	187.2	182.8	178.8
	4L_BS	188.0	184.6	180.8	177.2	174.6
	8L_BS	185.0	182.4	179.4	176.2	173.6
	16L_BS	183.8	181.4	178.8	176.2	173.4
	2L_RS	174.8	173.6	172.6	171.4	170.8
	4L_RS	179.4	177.6	175.8	174.2	172.4
	8L_RS	181.0	178.8	176.8	174.6	172.8
	16L_RS	181.6	179.6	177.2	174.8	172.8
RW+SW with additional consideration of Soil Temperature [T(RW+SW)]						
Soil Slope		**Slope Inclination Angle**				
		25°	**30°**	**35°**	**40°**	**45°**
Homogenous	**RS**	187.0	185.2	182.8	181.0	178.6
	BS	174.4	173.0	171.4	169.8	168.2
Reconstituted Varved Clay	**2L_BS**	196.0	192.4	188.4	184.0	180.0
	4L_BS	189.0	185.8	181.4	178.2	175.2
	8L_BS	186.0	183.4	180.4	177.4	174.8
	16L_BS	184.6	182.2	179.6	177.0	174.2
	2L_RS	174.2	173.2	172.4	170.8	169.8
	4L_RS	178.6	177.4	175.4	172.8	171.6
	8L_RS	180.2	178.6	176.4	173.8	172.4
	16L_RS	181.4	179.2	177.0	174.6	172.6

Furthermore, it can be observed from Table 5 that in the case of reconstituted varved slopes, the slope fails earlier as the number of laminae increases when BS is the topmost lamina. Conversely, when RS is the topmost lamina, the failure of the slope is delayed as the number of laminae increases. The above stated observations indicate the significant impact of the layering sequence on the stability and failure timing of the slopes.

Figure 11 illustrates the area of failed soil mass enclosed by the critical slip surface for all the considered slope profiles with a slope inclination angle of 30°. Notably, although the analysis is conducted under three different climatic conditions of RW, RW+SW, and T(RW+SW), the critical slip surface formed at failure remains similar across these conditions for a given slope inclination angle and soil profile. This is because different climatic conditions primarily affect the timing of slope failure, not the area of the soil mass affected by failure. However, the area of the failed soil mass does change with different slope inclination angles and soil profiles, which is discussed in the subsequent paragraph. Even for T(RW+SW), as discussed in Section 2.2, the representation of freezing as a change in water density does not influence the area of the failed slope mass. The area of the soil mass undergoing slope failure has been calculated as an average across all three climatic conditions, with the results listed in Table 6.

Among the homogeneous slope profiles (Figures 11a and 11b), the failed soil mass area is greater in the RS slope compared to the BS slope. For the reconstituted varved slopes (Figures 11c to 11j), the failed soil mass area for a 30° slope inclination angle is noticeably larger when RS occupies the topmost lamina compared to slopes where BS is the topmost lamina. For example, among 2L_BS and 2L_RS, it can be clearly seen that the area enclosed by the critical slip surface is more for 2L_RS than 2L_BS. Similarly, for other varved slopes, the failed area enclosed within the critical slip is more for 4L_RS, 8L_RS, and 16L_RS than for 4L_BS, 8L_BS, and 16L_BS, respectively. Similar observations of a smaller failed soil mass area in homogeneous BS slopes compared to homogeneous RS slopes, and a larger failed soil mass area in reconstituted varved clays with RS as the topmost layer, are consistent for all other slopes with inclination angles of 25°, 35°, 40°, and 45°, as listed in Table 6. For example, at a slope inclination angle of 30°, the area enclosed by the critical slip surface of the failed sliding mass is 28.60 m², 54.82 m², 64.77 m², and 69.15 m² for 2L_BS, 4L_BS, 8L_BS, and 16L_BS, respectively. In contrast, for 2L_RS, 4L_RS, 8L_RS, and 16L_RS, the corresponding areas are 74.19 m², 81.82 m², 80.01 m², and 76.67 m², which are substantially higher than the previous magnitudes.

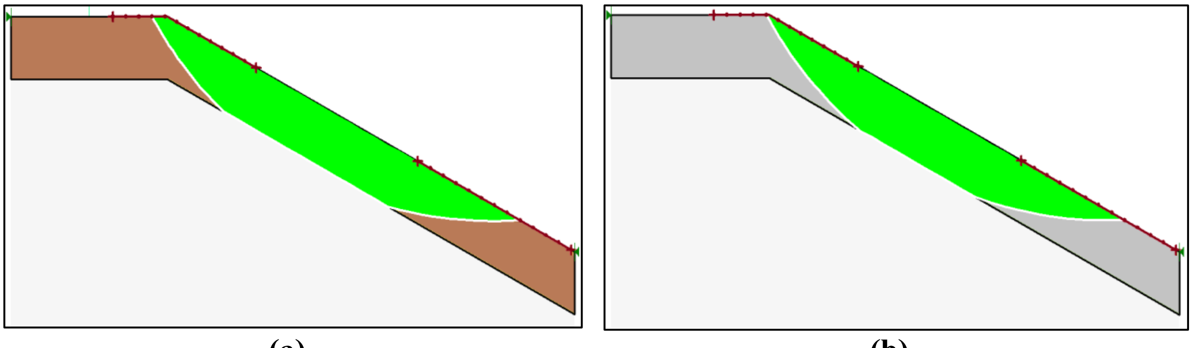

(a) (b)

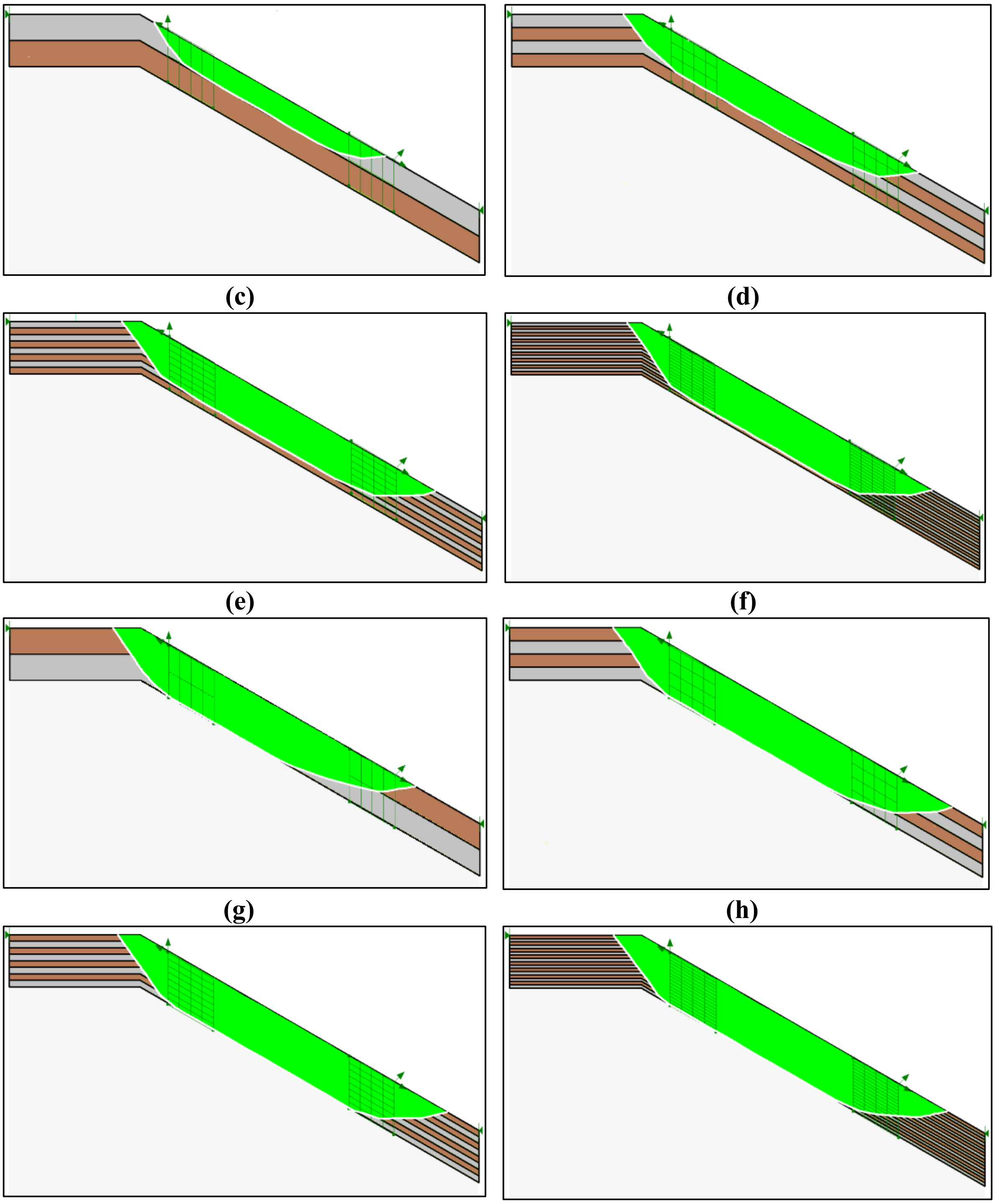

Figure 11. Failed soil mass enclosed in critical slip surface for 30° inclined slopes of (a) RS (b) BS (c) 2L_BS (d) 4L_BS (e) 8L_BS (f) 16L_BS (g) 2L_RS (h) 4L_RS (i) 8L_RS (j) 16L_RS

Table 6. Area enclosed by critical slip surface of the failed sliding mass (in m^2) for different combination of slope profiles and slope inclination angle

Slope Profiles	Slope Inclination Angles				
	25°	**30°**	**35°**	**40°**	**45°**
RS	114.26	74.19	61.50	55.71	43.90
BS	85.76	55.58	55.58	47.56	39.65
2L_BS	36.79	28.60	22.74	19.80	18.30
4L_BS	64.38	54.82	42.93	41.05	34.00
8L_BS	80.24	64.77	54.17	41.67	40.76
16L_BS	83.85	69.15	59.84	53.23	44.74
2L_RS	93.63	74.19	57.59	53.77	44.37
4L_RS	101.65	81.82	62.46	55.74	48.56
8L_RS	98.98	80.01	66.32	49.71	46.90
16L_RS	100.13	76.67	66.75	54.40	47.83

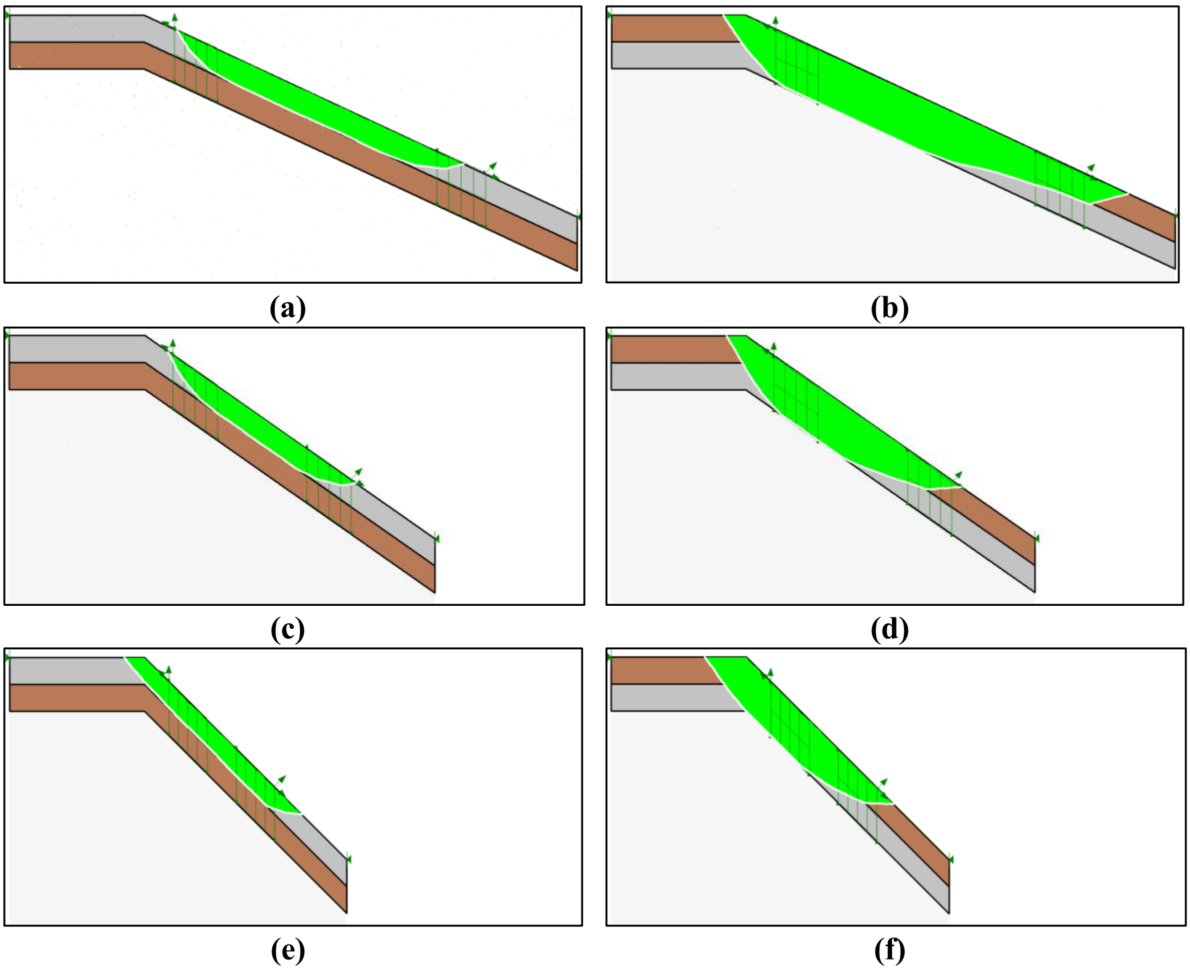

Figure 12. Failed soil mass within the critical slip surface formed in homogeneous and layered slopes of various inclinations (a) 25° inclined 2L_BS (b) 25° inclined 2L_RS (c) 35° inclined 2L_BS (d) 35° inclined 2L_RS (e) 45° inclined 2L_BS (f) 45° inclined 2L_RS

It is also observed from Table 6 that, for all the soil profiles considered in the analysis, the area of the failed soil mass decreases as the slope inclination angle increases. This is illustrated with the help of Figures 12 and 13, which shows the failed slopes in the case of 2-layered and 8-layered reconstituted varved slopes at inclination angles of 25°, 35°, and 45°. These figures demonstrate that as the slope inclination angle increases, the area involved in the slope failure decreases for the same slope profile.

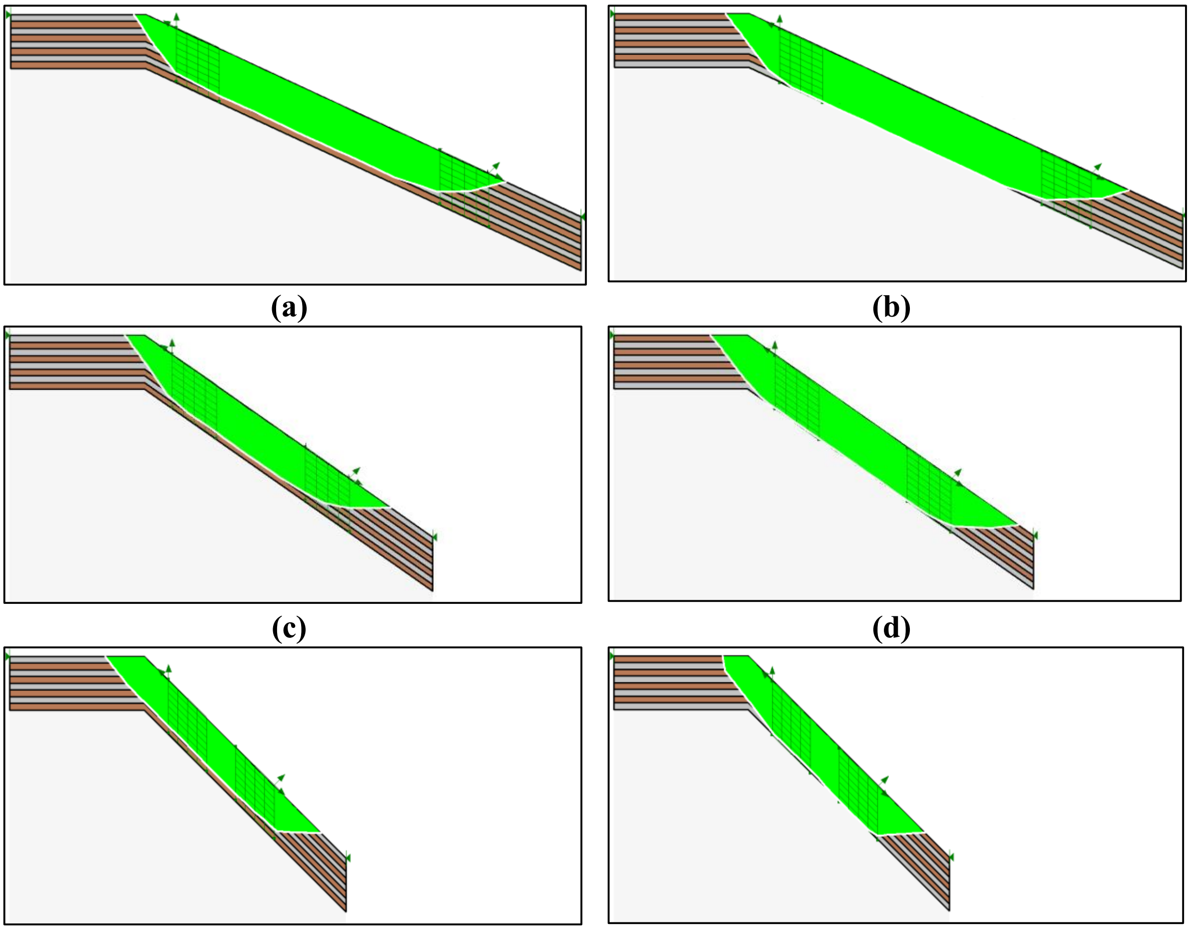

(a) (b) (c) (d) (e) (f)

Figure 13. Failed soil mass within the critical slip surface formed in homogeneous and layered slopes of various inclinations (a) 25° inclined 8L_BS (b) 25° inclined 8L_RS (c) 35° inclined 8L_BS (d) 35° inclined 8L_RS (e) 45° inclined 8L_BS (f) 45° inclined 8L_RS

3.2 Cumulative Net Infiltration and Cumulative Runoff into Different Soil Profiles for RW, RW+SW, and T(RW+SW) Scenarios

Figure 14 shows the magnitude of cumulative water infiltration into the slope over time for all the considered slope profiles at a slope inclination angle of 30°. Initially, before the commencement of the summer season, there is no infiltration. Infiltration begins in all soil profiles with the onset of summer season at 151 days, under all climatic conditions. Once water infiltration into the soil slope begins, its cumulative magnitude continues to increase with time. Eventually, the infiltration rates in all soil profiles reach their maximum values and remain constant for the remainder of the study period, up to 365 days. Although the rate of cumulative net infiltration in RW, RW+SW, and T(RW+SW) is different initially, the cumulative net infiltration approaches the same values over time for all slope profiles. This is because the porosity of given soil forming slope is same irrespective of the climatic condition. However, the time at which this maximum cumulative net infiltration is achieved varies for each slope profile under different climatic conditions, as shown in Table 7.

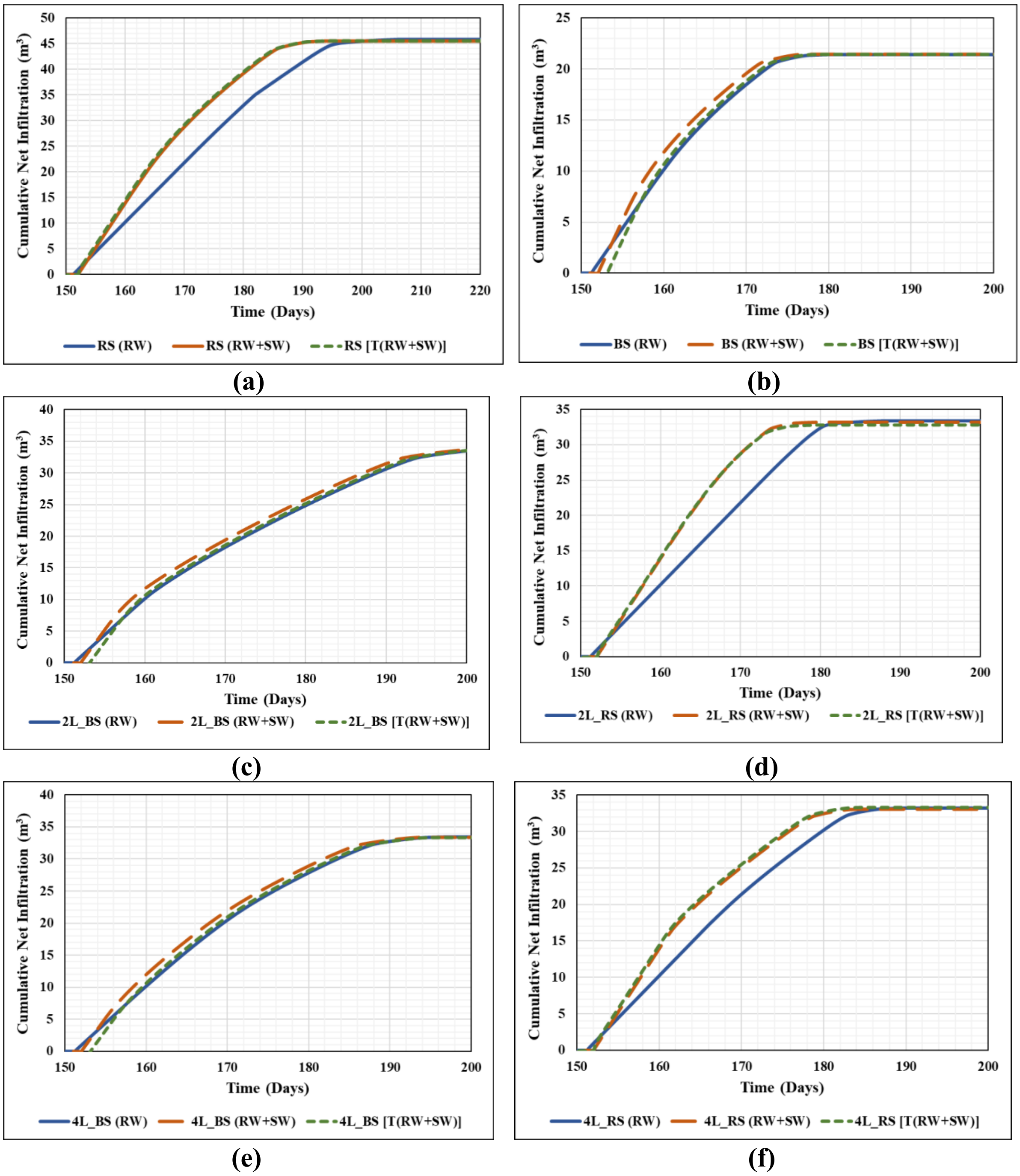

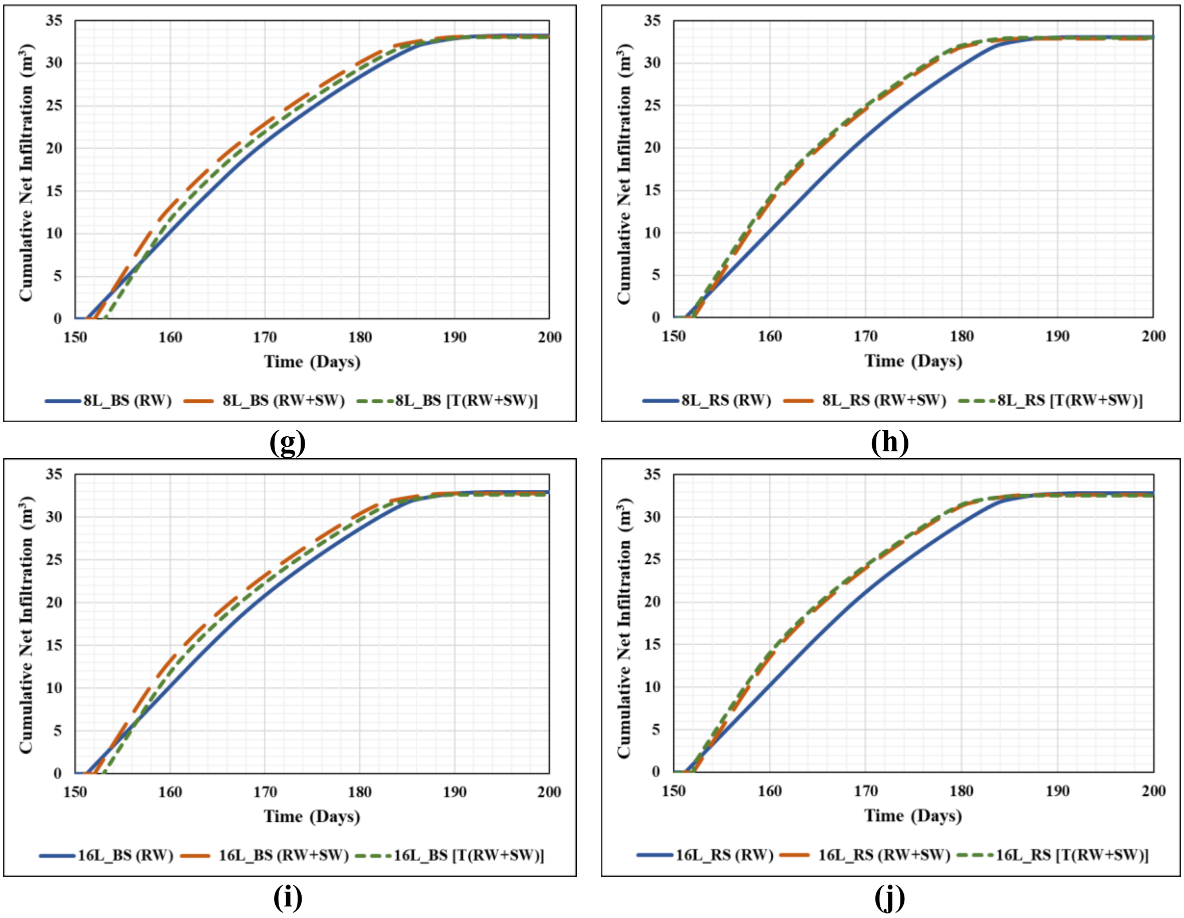

Figure 14. Variation in cumulative net infiltration with time in slope profiles with 30° slope inclination for RW, RW+SW and T(RW+SW) scenarios (a) RS (b) BS (c) 2L_BS (d) 2L_RS (e) 4L_BS (f) 4L_RS (g) 8L_BS (h) 8L_RS (i) 16L_BS (j) 16L_RS

From Figure 14, it is evident that the rate of cumulative net infiltration is higher for RW+SW and T(RW+SW) cases compared to RW climatic case. This is attributed to the additional water from snowmelt, along with rainwater, available for infiltration into the slope profiles. Furthermore, it is evident from the figure that the rate of cumulative net infiltration depends on the constituents of the slope and the sequential arrangement of the laminae in case of reconstituted varved clay slopes. Among homogeneous soil profiles of RS and BS, it can be observed that cumulative net infiltration in the RS slope profile is affected more than in the BS slope profile when additional water from snowmelt is considered in the analysis (Figures 14a and 14b). For reconstituted varved clay profiles, this additional snowmelt water appears to affect slope profiles with RS as the topmost lamina more significantly compared to the reconstituted varved profiles with BS as the topmost lamina (Figures 14c to 14j). This is evident from the difference in magnitudes of cumulative net infiltration at the same corresponding time period before the curves for RW+SW or T(RW+SW) and RW converge to the same magnitude of cumulative net infiltration. This observation of higher sensitivity in homogeneous RS slope profiles and reconstituted slope profiles with RS as the topmost laminae to infiltration, due to additional water from snowmelt, aligns with the observed higher sensitivity to FoS variation in these profiles, as discussed in Section 3.1.

Table 7. Duration (in days) until maximum cumulative net infiltration under different climatic conditions

Soil Slope		Slope Inclination Angle				
Water from Rain only [RW]						
Soil Slope		**25°**	**30°**	**35°**	**40°**	**45°**
Homogenous	**RS**	204.0	206.0	207.8	209.8	211.6
	BS	179.6	179.6	180.4	180.6	181.0
Reconstituted Varved Clay	**2L_BS**	203.2	202.4	201.8	201.2	201.0
	4L_BS	196.4	196.4	196.6	197.2	198.2
	8L_BS	194.2	194.4	195.0	195.6	196.2
	16L_BS	193.2	193.2	193.6	194.4	195.4
	2L_RS	186.6	187.8	188.8	190.4	191.4
	4L_RS	189.2	189.8	190.6	191.4	192.8
	8L_RS	190.6	191.0	191.6	192.8	194.0
	16L_RS	191.2	191.6	192.0	193.0	194.2
Water from both Rain and Snowmelt [RW+SW]						
Soil Slope		**25°**	**30°**	**35°**	**40°**	**45°**
Homogenous	**RS**	193.8	194.0	194.0	194.2	195.0
	BS	177.4	177.4	177.0	177.0	176.6
Reconstituted Varved Clay	**2L_BS**	201.2	200.4	200.2	200.0	199.8
	4L_BS	194.2	193.6	193.2	193.2	193.0
	8L_BS	191.2	190.8	190.0	189.6	189.4
	16L_BS	189.6	189.0	188.6	188.2	188.2
	2L_RS	179.4	180.0	180.2	180.8	181.6
	4L_RS	184.4	184.4	184.4	184.4	184.2
	8L_RS	186.2	186.0	185.8	185.8	185.4
	16L_RS	187.2	186.8	186.4	186.2	186.2
RW+SW with additional consideration of Soil Temperature [T(RW+SW)]						
Soil Slope		**25°**	**30°**	**35°**	**40°**	**45°**
Homogenous	**RS**	193.0	193.8	194.0	193.2	194.0
	BS	178.8	178.6	178.4	178.2	178.0
Reconstituted Varved Clay	**2L_BS**	202.4	201.4	201.2	201.0	200.8
	4L_BS	195.2	194.6	194.4	194.4	193.8
	8L_BS	192.2	191.4	191.0	190.4	190.4
	16L_BS	190.6	190.2	189.6	189.2	189.0
	2L_RS	179.2	179.8	180.2	178.8	181.2
	4L_RS	184.0	184.4	183.6	184.2	182.6
	8L_RS	185.8	186.0	185.0	184.8	185.0
	16L_RS	186.4	186.4	186.4	186.2	186.0

Table 7 provides valuable insights into the time when the maximum cumulative net infiltration is achieved. This information is crucial for understanding the dynamics of water infiltration in soil slopes and its impact on slope stability, particularly in the context of additional water from snowmelt. It is observed that Table 5 and Table 7 shows relationship between the time of slope failure and the time when maximum cumulative net infiltration is achieved in a given soil slope profile. For instance, under the RW climate scenario and at a slope inclination angle of 25°, the maximum and minimum durations to achieve cumulative net infiltration among all ten slope profiles are observed for the homogeneous RS (204.0 days) and BS slope profile (179.6 days), respectively. Now, from Table 5, for the same slope inclination of 25° under the RW climate condition, it can be observed that the maximum and minimum times for soil failure among all the slope profiles are taken by the homogeneous RS (196.2 days) and the BS slope profile (174.8 days), respectively. In the RW+SW scenario, Table 7 shows that 2L_BS and homogeneous BS take the maximum (201.2 days) and minimum (177.4 days) times to achieve maximum cumulative net infiltration, respectively, when the slope inclination angle is 25°. Correspondingly, Table 5 indicates that 2L_BS and homogeneous BS take the maximum (194.8 days) and minimum (173.2 days) times to fail. These observations suggest that water infiltration influences the timing of slope failure, with slopes failing before reaching maximum cumulative net infiltration. These observations are true for all slopes with different inclination angles.

From Table 7, it can further be observed that the time to attain maximum infiltration in 2L_BS, 4L_BS, 8L_BS, and 16L_BS is higher compared to 2L_RS, 4L_RS, 8L_RS, and 16L_RS under all climatic conditions. This trend matches the duration at which the slope failure occurs, with 2L_BS, 4L_BS, 8L_BS, and 16L_BS slopes failing later than 2L_RS, 4L_RS, 8L_RS, and 16L_RS for the respective climatic cases. Therefore, similar to how the soil constituting the ground surface or the topmost lamina governs slope failure as discussed in Section 3.1, a similar observation can be made regarding the sloping soil reaching its maximum infiltration capacity. From Table 7, it is further observed that when BS is the topmost lamina in the reconstituted slope, the time to reach maximum infiltration decreases as the number of laminae in the slope increases. Conversely, when the topmost layer is RS, the time to reach maximum infiltration is delayed with an increasing number of laminae. This trend is consistent across all climatic conditions and slope inclination angles. For example, under RW climatic conditions, for slopes inclined at 25°, the times to reach maximum infiltration are 203.2 days, 196.4 days, 194.2 days, and 193.2 days for 2L_BS, 4L_BS, 8L_BS, and 16L_BS, respectively. In contrast, for the sequential arrangement with RS as the top layer, these times are 186.6 days, 189.2 days, 190.6 days, and 191.2 days for 2L_RS, 4L_RS, 8L_RS, and 16L_RS, respectively. This trend in slope failure timing depending on the sequential arrangement in reconstituted slopes is also observed for other combinations of slope inclination angles and climatic conditions, as can be observed from Table 5.

Another observation drawn from Table 7 is regarding the effect of temperature across the soil slope profiles on cumulative net infiltration in the soil. The consideration of a temperature gradient across the soil profile induces freezing and thawing in slopes. It is observed that slope profiles with homogeneous RS and reconstituted varved slopes with RS as the topmost layer attain maximum cumulative infiltration earlier under T(RW+SW) climatic conditions compared to RW+SW conditions. In contrast, for other soil profiles with homogeneous BS and reconstituted slopes with BS as the topmost lamina, the maximum cumulative net infiltration is attained earlier under RW+SW conditions than under T(RW+SW). For instance, in the

RW+SW climatic case for homogeneous RS slope profiles, the maximum cumulative net infiltration is achieved at 193.8 days, 194 days, 194 days, 194.2 days, and 195 days for slope inclination angles of 25°, 30°, 35°, 40°, and 45°, respectively. Under T(RW+SW) conditions, the corresponding times are 193 days, 193.8 days, 194 days, 193.2 days, and 194 days, respectively. This earlier attainment of maximum cumulative infiltration under T(RW+SW) at all considered slope inclination angles is also observed for 2L_RS, 4L_RS, 8L_RS, and 16L_RS. As discussed previously in Section 3.1, slopes composed of homogeneous RS and reconstituted slopes with RS as the topmost lamina fail earlier under T(RW+SW) conditions compared to RW+SW conditions. Conversely, the reverse is true for homogeneous BS and reconstituted slopes with BS as the topmost lamina. These observations about slope failure and infiltration further reinforce the relationship between the time of slope failure and the infiltration characteristics of the respective soil slope profiles. The early attainment of maximum cumulative infiltration in homogeneous RS slope profiles and reconstituted varved clay profiles under T(RW+SW) compared to RW+SW can be attributed to the high thermal conductivity and heat capacity of RS, as discussed in detail in Section 3.2. These characteristics of RS results in the rapid melting of water in RS. This rapid melted water, along with incoming water from rain and snowmelt, results in the early attainment of maximum cumulative net infiltration in slopes with RS as the ground surface. Conversely, in the case of homogeneous BS and reconstituted slope profiles with BS as the topmost layer, the maximum cumulative net infiltration is achieved later under T(RW+SW) conditions compared to RW+SW. This delay is due to lower thermal conductivity and heat capacity, which results in slower melting of ice in the soil pores.

Figure 15 presents graphical plots of cumulative runoff over time for all soil profiles at a slope inclination angle of 30° at all three considered climatic conditions. It is observed that runoff begins at different times for different slope profiles under varying climatic conditions and continues throughout the study period. The graphs clearly show a notable rate of increase in cumulative runoff in the RW+SW and T(RW+SW) cases compared to RW, due to the additional water from snowmelt in the RW+SW and T(RW+SW) conditions. These observations are also valid for other slope inclination angles considered in this study. There is a small difference in the time at which runoff begins among the different slope profiles for RW and T(RW+SW), which can be observed from Table 8.

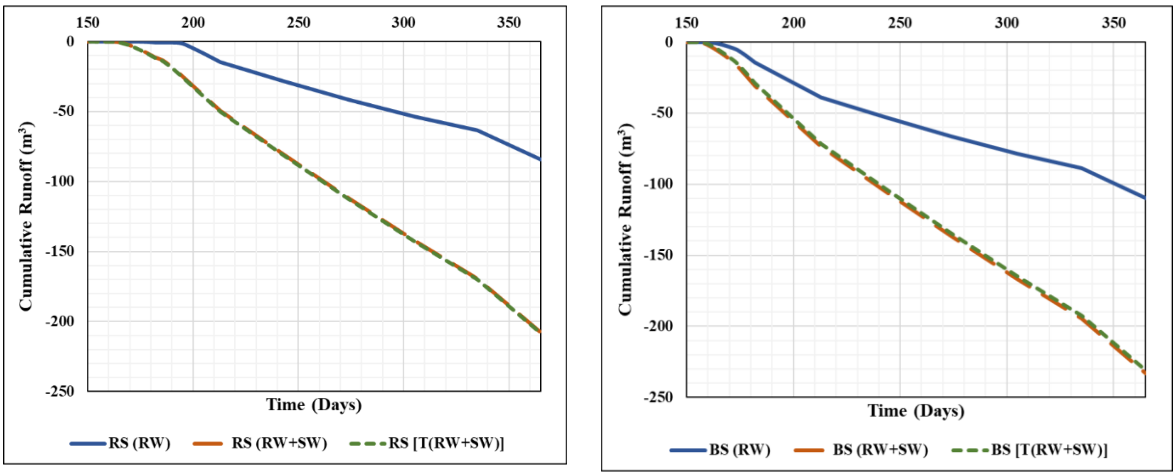

(a) (b)

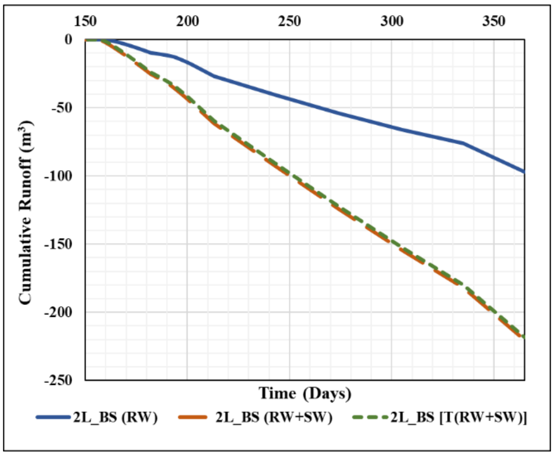
150
200
250
300
350
0
-50
-100
-150
-200
-250
Cumulative Runoff (m³)
Time (Days)
2L_BS (RW)
2L_BS (RW+SW)
2L_BS [T(RW+SW)]

(c)

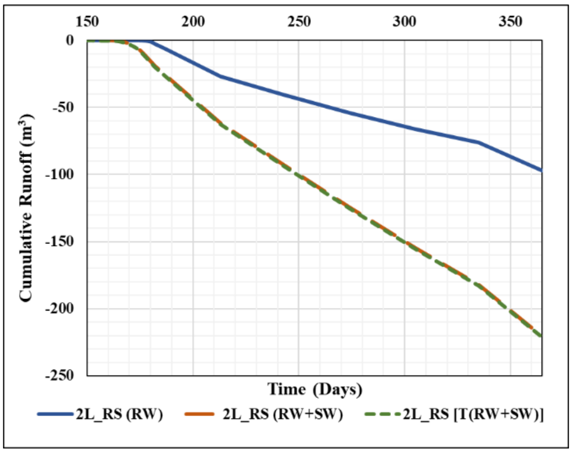
150
200
250
300
350
0
-50
-100
-150
-200
-250
Cumulative Runoff (m³)
Time (Days)
2L_RS (RW)
2L_RS (RW+SW)
2L_RS [T(RW+SW)]

(d)

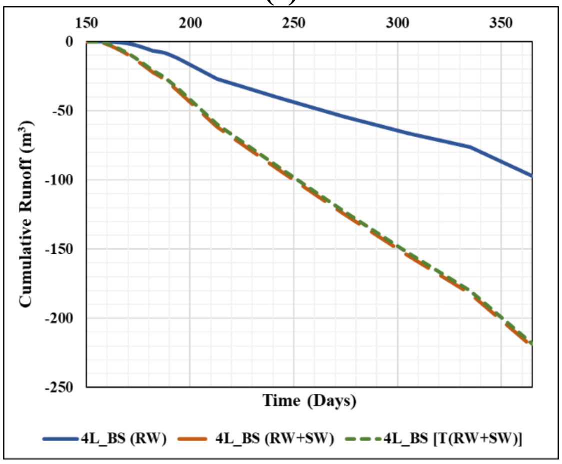
150
200
250
300
350
0
-50
-100
-150
-200
-250
Cumulative Runoff (m³)
Time (Days)
4L_BS (RW)
4L_BS (RW+SW)
4L_BS [T(RW+SW)]

(e)

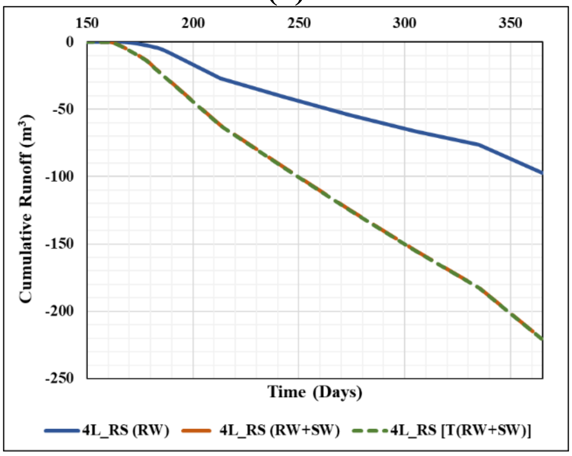
150
200
250
300
350
0
-50
-100
-150
-200
-250
Cumulative Runoff (m³)
Time (Days)
4L_RS (RW)
4L_RS (RW+SW)
4L_RS [T(RW+SW)]

(f)

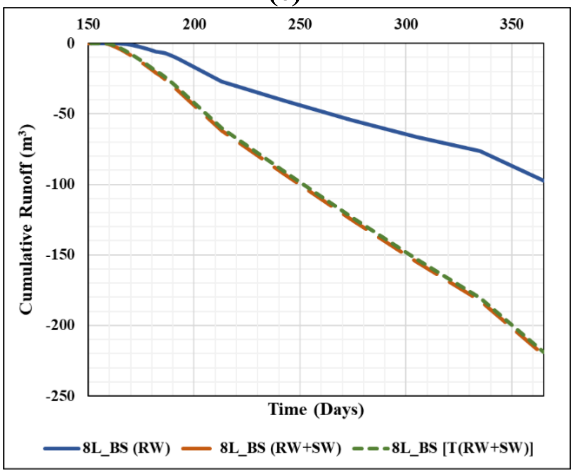
150
200
250
300
350
0
-50
-100
-150
-200
-250
Cumulative Runoff (m³)
Time (Days)
8L_BS (RW)
8L_BS (RW+SW)
8L_BS [T(RW+SW)]

(g)

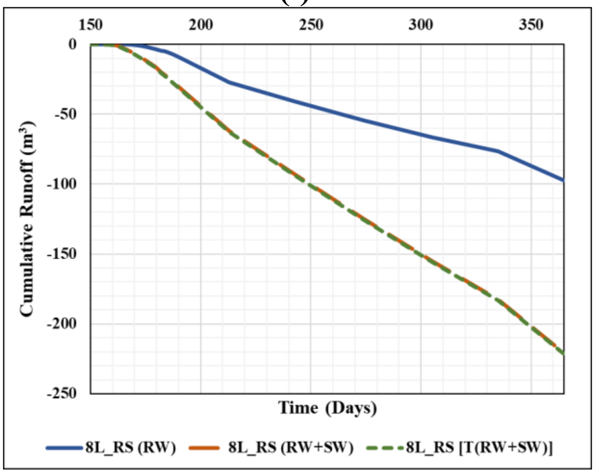
150
200
250
300
350
0
-50
-100
-150
-200
-250
Cumulative Runoff (m³)
Time (Days)
8L_RS (RW)
8L_RS (RW+SW)
8L_RS [T(RW+SW)]

(h)

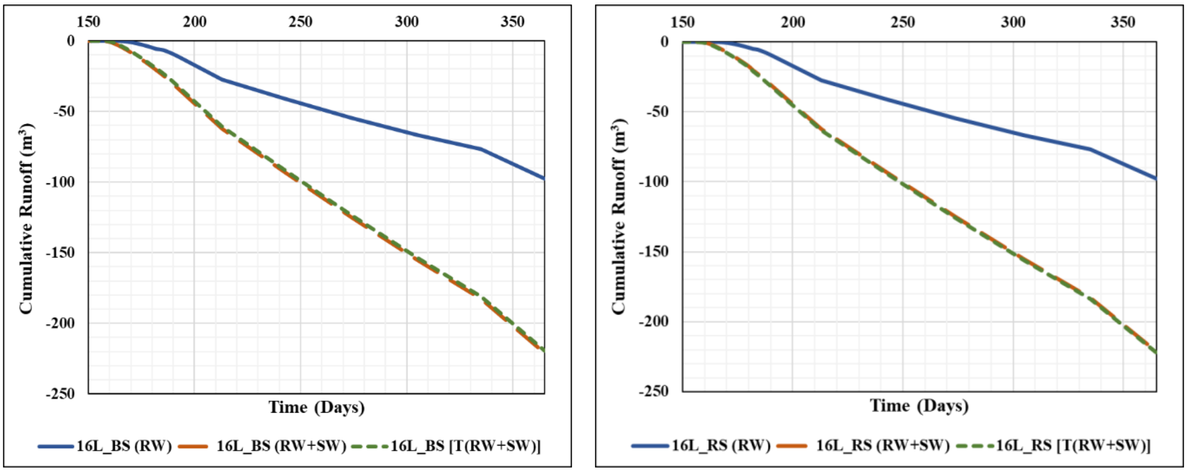

(i) **(j)**

Figure 15. Variation in cumulative runoff with time in slope profiles with 30° slope inclination for RW, RW+SW and T(RW+SW) scenarios (a) RS (b) BS (c) 2L_BS (d) 2L_RS (e) 4L_BS (f) 4L_RS (g) 8L_BS (h) 8L_RS (i) 16L_BS (j) 16L_RS

Table 8 shows the time at which runoff begins for the different slope profiles considered in this study. It can be seen from the table that in the RW+SW and T(RW+SW) cases, runoff begins earlier compared to the RW climate case. Among the RW+SW and T(RW+SW) cases, the time of runoff initiation depends on the soil constituting the ground surface, as observed in the infiltration and slope failure cases. Table 8 indicates that when the ground surface consists of RS, as in homogeneous RS slopes and reconstituted slopes with RS as the topmost lamina, runoff begins earlier in the T(RW+SW) climate compared to the RW+SW case. It is also noted that some of the runoff initiation times are identical due to the short data recording time interval of 0.2. The actual time difference between runoff initiation for these profiles might be less than 0.2 days, which may not be captured, resulting in the same recorded time values. For example, in the RW+SW case, the homogeneous RS slope profile shows runoff starting at 160.8 days for a 25° slope inclination and 160.6 days for the other inclinations (30°, 35°, 40°, and 45°). In the T(RW+SW) case, runoff starts at 152.4 days for slope inclinations of 25°, 30°, 35°, and 40°, and at 152.6 days for a 45° slope inclination. Similar early runoff initiation is observed for other profiles with RS as the topmost lamina. Conversely, for slopes with homogeneous BS and reconstituted slopes with BS as the topmost lamina, earlier runoff initiation is observed in the RW+SW case for all slope inclinations.

Tables 9(a) and 9(b) present the final magnitudes of cumulative net infiltration and cumulative runoff for different slope profiles at various inclination angles. These are the final magnitudes obtained at the end of the study period, which is the 365th day. The cumulative net infiltration and cumulative runoff magnitudes for all the reconstituted varved soil profiles have been found to be nearly similar, which is why the average of these magnitudes is taken and reported for different slope inclination angles. Additionally, the final cumulative net infiltration under all three climatic conditions of RW, RW+SW, and T(RW+SW) are same because the porosity remains same irrespective of the climatic conditions for a given slope profile and slope inclination angle. Therefore, only one magnitude of cumulative net infiltration exists for a given slope profile and slope inclination angle, and these magnitudes are mentioned in Table

9(a). However, the magnitude of the cumulative runoff at the end of the study period would differ between the climatic condition with only rainwater (RW) and those with additional water from snowmelt [RW+SW and T(RW+SW)]. The cumulative runoff magnitudes for both scenarios of water conditions are shown in Table 9(b).

Table 8. Duration (in days) until runoff initiation under different climatic conditions

Water from Rain only [RW]						
Soil Slope		**Slope Inclination Angle**				
		25°	**30°**	**35°**	**40°**	**45°**
Homogenous	**RS**	171.8	171.4	171.2	171.2	171.2
	BS	158.6	158.4	158.4	158.4	158.4
Reconstituted Varved Clay	**2L_BS**	158.6	158.4	158.4	158.4	158.4
	4L_BS	158.2	158.2	158.2	158.2	158.2
	8L_BS	161.6	161.4	161.4	161.2	161.2
	16L_BS	162.0	162.0	161.8	161.8	161.8
	2L_RS	172.2	172.0	171.8	171.6	171.6
	4L_RS	166.0	165.8	165.8	165.8	165.8
	8L_RS	164.8	164.6	164.6	164.6	164.6
	16L_RS	163.4	163.2	163.2	163.2	163.2
Water from both Rain and Snowmelt [RW+SW]						
Soil Slope		**Slope Inclination Angle**				
		25°	**30°**	**35°**	**40°**	**45°**
Homogenous	**RS**	160.8	160.6	160.6	160.6	160.6
	BS	155.4	155.4	155.4	155.4	155.4
Reconstituted Varved Clay	**2L_BS**	155.4	155.4	155.4	155.4	155.4
	4L_BS	155.2	155.2	155.2	155.2	155.2
	8L_BS	155.8	155.6	155.6	155.6	155.6
	16L_BS	156.4	156.4	156.4	156.4	156.4
	2L_RS	160.8	160.6	160.6	160.6	160.6
	4L_RS	160.4	160.2	160.2	160.2	160.2
	8L_RS	157.6	157.6	157.0	157.6	157.6
	16L_RS	157.2	157.2	157.2	157.2	157.2
RW+SW with additional consideration of Soil Temperature [T(RW+SW)]						
Soil Slope		**Slope Inclination Angle**				
		25°	**30°**	**35°**	**40°**	**45°**
Homogenous	**RS**	152.4	152.4	152.4	152.4	152.6
	BS	156.4	156.4	156.4	156.4	156.4
Reconstituted Varved Clay	**2L_BS**	156.4	156.4	156.4	156.4	156.4
	4L_BS	156.2	156.2	156.2	156.2	156.2
	8L_BS	156.6	156.6	156.6	156.6	156.6
	16L_BS	157.2	157.2	157.2	157.2	157.2
	2L_RS	152.4	152.4	152.4	152.4	152.4
	4L_RS	152.6	152.6	152.4	152.6	152.6
	8L_RS	152.4	152.4	152.4	152.4	152.4
	16L_RS	156.8	155.2	155.2	155.2	155.6

Table 9(a). Cumulative net infiltration (m^3) at the end of study period in different slope profiles

Slope Profiles	Slope Inclination Angle				
	25°	**30°**	**35°**	**40°**	**45°**
Homogenous RS	53.33	45.61	39.79	35.36	31.68
Homogenous BS	25.12	21.43	18.71	16.60	14.88
Reconstituted Varved Clays	38.72	33.12	28.92	25.59	23.02

Table 9(b). Cumulative runoff (m^3) at the end of study period in different slope profiles

Water from Rain only [RW]					
Slope Profiles	**Slope Inclination Angle**				
	25°	**30°**	**35°**	**40°**	**45°**
Homogenous RS	99.46	107.18	113.00	117.43	121.11
Homogenous BS	129.08	132.77	135.49	137.6	139.32
Reconstituted Varved Clays	114.70	120.30	124.50	127.83	130.40
Additional Water from Snowmelt alongside Rainwater [RW+SW and T(RW+SW)]					
Slope Profiles	**Slope Inclination Angle**				
	25°	**30°**	**35°**	**40°**	**45°**
Homogenous RS	244.76	252.48	258.3	262.73	266.41
Homogenous BS	272.40	276.09	278.81	280.92	282.64
Reconstituted Varved Clays	259.06	264.66	268.86	272.19	274.76

From Table 9(a), it is evident that as the slope inclination angle increases, the cumulative net infiltration decreases for all slope profiles. This decrease is attributed to the reduced length of the sloping ground with the increase in slope angle, resulting in a smaller area available for water to infiltrate into the soil and, consequently, fewer pores to retain water. As a result, the excess water that is not retained within the soil contributes to runoff. Thus, as the slope inclination angle increases, the magnitude of cumulative runoff also increases, as observed from Table 9(b). Furthermore, Table 9(a) shows that the maximum and minimum infiltration occurs in homogeneous RS and homogeneous BS slope profiles, respectively, across various slope inclination angles. For example, at a slope inclination angle of 25°, the cumulative net infiltration at the end of the study period is 53.33 m^3 for homogeneous RS, 25.12 m^3 for homogeneous BS, and 38.72 m^3 for reconstituted varved slopes. The higher cumulative net infiltration in homogeneous RS slopes compared to homogeneous BS slopes is due to RS having a higher porosity of 0.42 compared to 0.37 for BS, as shown in Table 2, which allows RS to retain more water. From Table 9(b), it can be seen that cumulative runoff is higher when additional water from snowmelt is considered along with rainwater, compared to when only rainwater is considered. It can be further observed that the cumulative runoff is maximum for homogeneous BS and minimum for homogeneous RS for all slope inclination angles under both water conditions. For instance, at a slope inclination angle of 25° and when only rainwater is considered, the cumulative runoff is 224.62 m^3 for homogeneous BS, 196.33 m^3 for homogeneous RS, and 210.94 m^3 for reconstituted varved slopes. The cumulative net infiltration and cumulative runoff for reconstituted varved slopes fall between the values observed for homogeneous RS and homogeneous BS slope profiles. These observations regarding net cumulative infiltration and cumulative runoff also hold true for slopes with different inclination angles, given the same soil profile.

4. Conclusions

The present study employs a FE numerical modeling transient analysis approach to investigate the complex consequences of hydrological changes on slope stability and water balance for different slope profiles under three climatic conditions of RW, RW+SW, and T(RW+SW). The study considers ten slope profiles, which includes homogeneous slopes composed of RS and BS, as well as reconstituted varved clay profiles with alternating layers, which includes 2L_BS, 4L_BS, 8L_BS, 16L_BS, 2L_RS, 4L_RS, 8L_RS, and 16L_RS. These profiles are analyzed at five slope inclination angles of 25°, 30°, 35°, 40°, and 45°. Key observations from the study include:

- When additional water from snowmelt is considered alongside rainwater, slopes tend to fail earlier (approximately 5-15 days quicker than slopes subjected to only rainwater), with earlier attainment of maximum cumulative net infiltration and initiate runoff earlier. Furthermore, as the slope inclination angle increases from 25º to 45º, the slope fails sooner (nearly 6-10 days earlier for the steeper inclinations), and the area of soil mass involved in the failure decreases (in the tune of 50% for the steepest slope as compared to the flatter ones considered in the study). This trend is consistent for all slope profiles, although the magnitudes of each variable differ.
- Among homogeneous slopes of RS and BS, the latter fail earlier (nearly 15-20 days earlier) under all the considered climatic conditions and slope inclinations. This is attributed to the relatively lower shear strength parameters of BS.
- The time to slope failure in reconstituted varved clay slopes with alternating RS and BS layers is governed by the composition of topmost lamina. Reconstituted varved clay slopes with RS as the topmost lamina fail earlier by nearly 15 days than those with BS as the topmost lamina.
- The time to slope failure is well correlated with the time to reach maximum cumulative net infiltration. The more time it takes to reach maximum cumulative net infiltration, the longer it takes for the slope to fail, although slope failure always occurs before maximum cumulative infiltration is reached. This correlation between slope failure and maximum cumulative net infiltration holds true for all slope profiles at all slope inclination angles.
- For any inclination angle, layered slopes with RS as the topmost layer generate deeper slip surfaces and involve a larger area of failed soil mass, which is nearly double as compared to slopes with BS as the topmost lamina.
- Temperature gradient within the slope profile influences its stability and water dynamics. Homogeneous RS slopes and reconstituted varved slopes with RS as the topmost layer fail earlier (by nearly 15 to 20 days) under T(RW+SW) conditions as compared to RW+SW, while BS slopes and those with BS as the topmost layer fail earlier under RW+SW

conditions. This is attributed to the higher thermal conductivity and specific heat capacity of RS.

As can be understood from the conclusions, the depth and extent of the failure will largely be governed by the topmost laminae. In case RS forms the topmost laminae, the severity of the landslide would be much higher than when BS forms the topmost laminae. As the glacial depositions occur over the cycles of freezing and thawing, there would be alternate periods of red soil and black soil forming the topmost lamina. Hence, in such situation, the periods in which RS forms the topmost layer, the possibility of the slope failure would be highest and that too occurring with a higher hazard quotient. Comparatively, the periods that would have BS as the topmost lamina, the extent and severity of the landslides would be comparatively lesser.

Finally, it can be inferred from the study that the ground surface of the slope, through which land-climate interactions primarily occur, plays a major role in governing slope stability, water infiltration into the slope, and the volume of water contributing to runoff. The present study highlights the complex interactions among soil composition, the sequential arrangement of laminae, and their influence on slope stability, infiltration, and runoff under varying water flux scenarios and different climatic conditions. This research is particularly relevant to glaciated regions, where freezing and thawing of soils and rapid snowmelt due to climate change significantly alter the hydrological dynamics of the area. These altered dynamics lead to increased water volumes that contribute to both infiltration and runoff, potentially triggering early slope instabilities. The study specifically emphasizes the effects of laminae arrangement and the number of laminae in varved deposits on slope stability and hydrological behavior in glacial regions. The findings underscore the need to incorporate detailed climatic conditions and laminae composition in case of layered soil slope during slope stability assessments and water balance studies in such environments. This understanding is crucial for effective water management and predicting the occurrence of landslides in these regions.

5. Declarations

Funding: This study belongs to a part of the project 'Study of Glacial Dynamics and Sustainable Hydrological Resources in Arunachal Himalaya' (Project No. DST/CCP/MRDP/185/2019(G) dated 13/03/2020). The project is supported by Department of Science & Technology (SPLICE – Climate Change Program), Ministry of Science and Technology, Govt. of India. The authors express their gratitude for receiving the financial support for the same.

Conflict of Interest: The authors declare that they have no known competing financial interests or personal relationships that could have appeared to influence the work reported in this paper.

Data Availability Statement: The data pertaining to and reported in this study is available from the corresponding author upon reasonable request.

Consent to Participate: Not applicable

Consent to Publish: Not applicable

Ethics Approval: Not applicable

Author Contributions: DA was involved in conceptualization, formal analysis and originally writing the main manuscript, preparation of revised manuscript and review response; AD was involved in supervision, revision and editing of drafted manuscript, reviewing the revised manuscript and review response; RK was involved in supervision. All authors reviewed the manuscript.

References

[1] Shazan, M., Pandit, K., Sarkar, S., Uniyal, P. (2023). A brief review on landslides in Indian Himalayas. Conference: Innovative and Sustainable Materials & Technologies (ISCMT2023), At: New Delhi, India.

[2] Fayaz, M., Meraj, G., Khader, S.A., Farooq, M. (2022). ARIMA and SPSS statistics based assessment of landslide occurrence in western Himalayas. Environmental Challenges, 9:100624. https://doi.org/10.1016/j.envc.2022.100624

[3] Choudhury, D., Das, T., Rao, V. D. (2023). Case studies and numerical investigation of landslide triggering mechanisms in Western Ghats, Kerala, India. Indian Geotechnical Journal, 54: 96-108. https://doi.org/10.1007/s40098-023-00763-y

[4] Aziz, K., Mir, R.A., Ansari, A. (2024). Precision modeling of slope stability for optimal landslide risk mitigation in Ramban road cut slopes, Jammu and Kashmir (J&K) India. Modeling Earth Systems and Environment, 10(3): 1-17. https://doi.org/10.1007/s40808-023-01949-2

[5] Dai, G., Zhang, F., Wang, Y. (2022). Stability analysis of layered slopes in unsaturated soils. Frontiers of Structural and Civil Engineering, 16: 378–387. https://doi.org/10.1007/s11709-022-0808-2

[6] Chatterjee, D., Murali Krishna, A. (2021). Stability analysis of two-layered non-homogeneous slopes. International Journal of Geotechnical Engineering, 15(5): 617–623. https://doi.org/10.1080/19386362.2018.1465686

[7] Sarkar, S., Chakraborty, M. (2021). Stability analysis for two-layered slopes by using the strength reduction method. International Journal of Geo-Engineering, 12(24). https://doi.org/10.1186/s40703-021-00153-4

[8] Zhou, H., Hu, Q., Yu, X., Zheng, G., Liu, X., Xu, H., Yang, S., Liu, J., Tian, K. (2023). Quantitative bearing capacity assessment of strip footings adjacent to two-layered slopes considering spatial soil variability. Acta Geotechnica, 18, 6759–6773. https://doi.org/10.1007/s11440-023-01875-8

[9] Gan, J., Zhang, Y.X. (2020). Analysis of model tests of rainfall-induced soil deposit landslide. Advances in Civil Engineering, (3): 1-13. https://doi.org/10.1155/2020/6431247

[10] Wang, J. J., Zhang, H.P., Zhang, L., Liang, Y. (2012). Experimental study on heterogeneous slope responses to drawdown. Engineering Geology, 147-148: 52–56. https://doi.org/10.1016/j.enggeo.2012.07.020.

[11] Liu, H. X., Xu, Q., Li, Y.R. (2014). Effect of lithology and structure on seismic response of steep slope in a shaking table test. Journal of Mountain Science, 11 (2): 371–383. https://doi.org/10.1007/s11629-013-2790-6.

[12] Chok, Y. H., Jaksa, M.B., Kaggwa, W.S., Griffiths, D.V., Fenton, G.A. (2016). Neural network prediction of the reliability of heterogeneous cohesive slopes. International Journal for Numerical and Analytical Methods in Geomechanics, 40 (11): 1556–1569. https://doi.org/10.1002/nag.2496.

[13] Deng, Do-pi., Li, L., Zhao, Li-he. (2019). Stability analysis of a layered slope with failure mechanism of a composite slip surface. International Journal of Geomechanics, 19(6). https://doi.org/10.1061/(ASCE)GM.1943-5622.0001417

[14] Wu, L. Z., Huang, R. Q., Li, H. L., Li, X., Sun, P. (2021). The model tests of rainfall infiltration in two-layer unsaturated soil slopes. European Journal of Environmental and Civil Engineering, 25(9): 1555–1569. https://doi.org/10.1080/19648189.2019.1585961

[15] Tang, J., Taro, U., Huang, D., Xie, J., Tao, S. (2020). Physical model experiments on water infiltration and failure modes in multi-layered slopes under heavy rainfall. Applied Sciences, 10(10): 3458. https://doi.org/10.3390/app10103458

[16] Irfan, M., Akbar, A., Aziz, M., Khan, A.H. (2013). A parametric study on stability of open excavations in alluvial soils of Lahore District, Pakistan. Geotechnical and Geological Engineering, 31: 729–738. https://doi.org/10.1007/s10706-013-9623-9

[17] Weng, C.K. (2009). Effect of layering on slope instability induced by rainfall. Masters Thesis. Universiti Teknologi Malaysia.

[18] Wang, T., Jia, H., Sun, Q., Li, G. (2022). Effect of the frozen layer on the stability of cut soil slopes during seasonal freezing and thawing. Research in Cold and Arid Regions, 14(5): 281-292. https://doi.org/10.1016/j.rcar.2022.12.001

[19] Li, M., Chen, S.F. (2016). Analysis on stability of slope in a typical cold region based on thermo-mechanical coupling. Bulgarian Chemical Communications, Special Edition F: 96-103.

[20] Chen, H., Yuan, X., Liu, W. (2021). Study on the stability of highway slope in cold region under freeze-thaw cycles. E3S Web of Conferences 248(1):03046. https://doi.org/10.1051/e3sconf/202124803046

[21] Hartemink, A.E., Zhang, Y., Bockheim, J.G., Curi, N., Silva, S.H.G., Grauer-Gray, J., Lowe, D.J., Krasilnikov, P. (2020). Soil horizon variation: A review. Chapter 3 in Advances in Agronomy, 160(1): 125-185. https://doi.org/10.1016/bs.agron.2019.10.003

[22] Reddy, D.V. (2014). Landslides-debris flows floods earthquakes and tsunamis of indian sub-continent- emergency preparedness plan – A typical analysis. 3rd World Conference on Applied Sciences, Engineering & Technology 27-29 September 2014, Kathmandu, Nepal. http://doi.org/10.13140/2.1.1942.5286

[23] Dikshit, A., Sarkar, R., Pradhan, B., Segoni, S., Alamri, A.M. (2020). Rainfall induced landslide studies in Indian Himalayan region: A critical review. Applied Sciences, 10(7), 2466. https://doi.org/10.3390/app10072466

[24] Kansal, M.L., Singh, S. (2022). Flood management issues in hilly regions of Uttarakhand (India) under changing climatic conditions. Water, 14(12): 1879. https://doi.org/10.3390/w14121879

[25] Singh, S.P., Reshi, Z.A., Joshi, R. (2023). Treeline research in the Himalaya: Current understanding and future imperatives. In: Singh, S.P., Reshi, Z.A., Joshi, R. (eds) Ecology of Himalayan Treeline Ecotone. Springer, Singapore. https://doi.org/10.1007/978-981-19-4476-5_1.

[26] Anderson, R.Y., Dean, W.E. (1988). Lacustrine varve formation through time. Palaeogeography, Palaeoclimatology, Palaeoecology, 64(1-4): 215-235. https://doi.org/10.1016/0031-0182(88)90055-7

[27] Shur, Y., Zhestkova, T. (2003). Cryogenic structure of a glacio-lacustrine deposit. Permafrost, Phillips, Springman & Arenson (eds), 1051-1056.

[28] Netto, R.G., Benner, J. S., Buatois, L.A., Uchman, A., Mangano, M.G., Ridge, J.C., Kazakauskas, Gaigalas, A. (2012). Glacial Environments. Chapter-11 of Developments in Sedimentology, 64: 299-327. https://doi.org/10.1016/B978-0-444-53813-0.00011-3

[29] Palmer, A.P., Bendle, J.M., MacLeod, A., Rose, J., Thorndycraft, V.R. (2019). The micromorphology of glaciolacustrine varve sediments and their use for reconstructing palaeoglaciological and palaeoenvironmental change. Quaternary Science Reviews, 226: 105964. https://doi.org/10.1016/j.quascirev.2019.105964

[30] Vergnano, A., Oggeri, C., Godio, A. (2023). Geophysical–geotechnical methodology for assessing the spatial distribution of glacio-lacustrine sediments: The case history of Lake Seracchi. Earth Surface Processes and Landforms, 48(7): 1374-1397. https://doi.org/10.1002/esp.5555

[31] Wang, H., Yang, A., Jiang, S., Liu, N. (2023). Reconstruction of a Holocene landslide-dammed lake in the Yalong basin, eastern Tibetan Plateau. Geohazards and Georisks, 10. https://doi.org/10.3389/feart.2022.1042581

[32] Ahmad, N., Hashimi, N. (1974). Glacial history of Kolahoi glacier, Kashmir, India. Journal of Glaciology, 13(68): 279-283. http://doi.org/10.3189/S002214300002308X

[33] Pant, R. K., Juyal, N., Rautela, P., Yadav, M. G., Sangode, S. J. (1998). Climate instability during last glacial stage: Evidence from varve deposits at Goting, district Chamoli, Garhwal Himalaya, India. Current Science, 75(8): 850–855. http://www.jstor.org/stable/24101637

[34] Juyal, N., Pant, R.K., Basavaiah, N., Bhushan, Jain, M., Saini, N.K., Yadava, M.G., Singhvi, A.K. (2009). Reconstruction of last glacial to early Holocene monsoon variability from relict lake sediments of the Higher Central Himalaya, Uttarakhand, India. Journal of Asian Earth Sciences, 34(3): 437-449. https://doi.org/10.1016/j.jseaes.2008.07.007

[35] Bhattacharyya, A., Ranhotra, P.S., Gergan, J.T. (2011). Vegetation vis-à-vis climate and glacier history during 12,400 to 5,400 yr BP from Dokriani valley, Garhwal Himalaya, India. Journal of Geological Society of India, 77: 401–408. https://doi.org/10.1007/s12594-011-0047-y

[36] Beukema, S., Krishnamurthy, R., Juyal, N., Basavaiah, N., Singhvi, A. (2011). Monsoon variability and chemical weathering during the late Pleistocene in the Goriganga basin, higher central Himalaya, India. Quaternary Research, 75(3): 597-604. https://doi.org/10.1016/j.yqres.2010.12.016

[37] IS:2720 Part 5 (1985). Methods of test for soils: Determination of liquid limit and plastic limit. Bureau of Indian Standards, New Delhi, India.

[38] IS:2720 Part 4 (1980). Methods of test for soils: Grain size analysis. Bureau of Indian Standards, New Delhi, India.

[39] Eden, W.J. (1955). Laboratory study of varved clay from Steep Rock Lake, Ontario. American Journal of Science, 253: 659-674. https://doi.org/10.4224/20331506

[40] Kazi, A. (1967). Aspects of the engineering geology of laminated glacial lake clays. Ph.D. Thesis, Imperial College of Science London.

[41] Eigenbrod, K.D., Burak, J.B. (1991). Effective stress paths and pore-pressure responses during undrained shear along the bedding planes of varved Fort William Clay. Canadian Geotechnical Journal, 28 (6): 804-811. https://doi.org/10.1139/t91-097

[42] Lydzba, D., Tankiewicz, M. (2012). Preliminary study of failure anisotropy characterization of varved clay. AGH Journal of Mining and Geoengineering, 36 (2): 229-234.

[43] Florkiewicz, A., Flieger-Szymanska, M., Machowiak, K., Wanatowski, D. (2014). Engineering properties of varved clays from the Junikowski Stream Valley in Poland. Conference: Proc. 4th International Conference on Geotechnical Engineering for Disaster Mitigation and Rehabilitation (4th GEDMAR) At: Kyoto, Japan Volume: Geotechnics for Catastrophic Flooding Events

[44] Tankiewicz, M. (2016). Structure investigations of layered soil-varved clay. Annals of Warsaw University of Life Sciences-SGGW. Land Reclamation, 48: 365 - 375. http://doi.org/10.1515/sggw-2016-0028

[45] Krawczyk, D., Szymanska, M.F. (2018). The value of plasticity index (IP) and liquidity index (IL) of North Polish ablation boulder clays and varved clays depending of the method of its determination. Scientific Review – Engineering and Environmental Sciences, 27 (2): 167–174. https://doi.org/10.22630/PNIKS.2018.27.2.16

[46] Flieger-Szymanska, M., Machowiak, K., Krawczyk, D., Wanatowski, D. (2019). Characterisation of mineral composition and strength parameters of varved clays. In: Proceedings of the 17th European Conference on Soil Mechanics and Geotechnical Engineering (ECSMGE 2019). XVII ECSMGE 2019, 01-06 Sep 2019, Reykjavik, Iceland. International Society for Soil Mechanics and Geotechnical Engineering. ISBN 978-9935-9436-1-3

[47] IS:2720 Part 3/Sec-2 (1980). Methods of test for soils: Determination of specific gravity - Part 3/Section 2: Fine, medium, and coarse-grained soils. Bureau of Indian Standards, New Delhi, India.

[48] IS:2720 Part 7 (1980). Methods of test for soils: Determination of water content-dry density relation using light compaction. Bureau of Indian Standards, New Delhi, India.

[49] ASTM. 2012. Standard test method for direct shear test of soils under consolidated drained conditions. ASTM D3080/D3080M. West Conshohocken, PA: ASTM.

[50] ASTM. 2015. Standard test method for measurement of hydraulic conductivity of porous material using a rigid-wall, compaction-mold permeameter. D5856−15.

[51] Irfan, M., Rasool, A. M., Aziz, M., Ali, U., Niazi, F., Uchimura, T. (2024). Development of Wetting-Drying Curves from Elastic Wave Velocities Using a Novel Triaxial Test Apparatus. Studia Geotechnica et Mechanica, 46(2): 111-124. https://doi.org/10.2478/sgem-2024-0006

[52] ASTM. 2002. Standard test method for determination of the soil water characteristic curve for desorption using a hanging column, pressure extractor, chilled mirror hygrometer, and/or centrifuge, D 6836-02, American Society of Testing Materials. D6836 Method D.

[53] van Genuchten, M. Th. (1980). A closed-form equation for predicting the hydraulic conductivity of unsaturated soils. Soil Science Society of American Journal, 44: 892-898. https://doi.org/10.2136/sssaj1980.03615995004400050002x

[54] Rasool, A. M., Aziz, M. (2019). Shear infiltration and constant water content tests on unsaturated soils. Geomechanics and Engineering, 19(5): 435-445. https://doi.org/10.12989/gae.2019.19.5.435

[55] Zhang, L., Yang, C., Wang, D., Zhang, P., Zhang, Y. (2022). Freezing point depression of soil water depending on its non-uniform nature in pore water pressure. Geoderma, 412: 115724. https://doi.org/10.1016/j.geoderma.2022.115724

[56] Drotz, S.H., Tilston, E.L., Sparrman, E.L., Schleucher, J., Nilsson, M., Oquist, M. G. (2009). Contributions of matric and osmotic potentials to the unfrozen water content of frozen soils. Geoderma, 18(2-4): 392-398. https://doi.org/10.1016/j.geoderma.2008.11.007

[57] Zhang, S., Teng, J., He, Z., Sheng, D. (2016). Importance of vapor flow in unsaturated freezing soil. A numerical study. Cold Region Science and Technology, 126: 1-9. https://doi.org/10.1016/j.coldregions.2016.02.011

[58] KD2 Pro. (2008). KD2 Pro thermal properties analyzer operators manual, version 8. Pullman, WA: Decagon Devices.

[59] ASTM. 2014. Standard test method for determination of thermal conductivity of soil and soft rock by thermal needle probe procedure. D5334. Standard, American Society for Testing and Materials.

[60] Campbell, G. S., Calissendorff, C., Williams, J.H. (1991). Probe for measuring soil specific heat using a heat-pulse method. Soil Science Society of America Journal, 55 (1): 291–293. https://doi.org/10.2136/sssaj1991.03615995005500010052x

[61] Cai, G., T. Zhang, A. J., Puppala, S. Liu. (2015). Thermal characterization and prediction model of typical soils in Nanjing area of China. Engineering Geology, 191: 23–30. https://doi.org/10.1016/j.enggeo.2015.03.005

[62] Bračko, T., Žlender, B., Jelušič, P. (2022). Implementation of climate change effects on slope stability analysis. Applied Sciences, 12(16): 8171. https://doi.org/10.3390/app12168171

[63] Chuaiwate, P., Jaritngam, S., Panedpojaman, P., Konkong, N. (2022). Probabilistic analysis of slope against uncertain soil parameters. Sustainability, 14(21): 14530. https://doi.org/10.3390/su142114530

[64] Elahi, T. E., Islam, M. A., Islam, M. S. (2022). Parametric assessment of soil nailing on the stability of slopes using numerical approach. Geotechnics, 2(3): 615-634. https://doi.org/10.3390/geotechnics2030030

[65] Kim, Y., Rahardjo, H., Nistor, M.M., Satyanaga, A., Leong, En-Ch, Sham, A.W.L. (2022). Assessment of critical rainfall scenarios for slope stability analyses based on historical rainfall records in Singapore. Environmental Earth Sciences, 81(1). https://doi.org/10.1007/s12665-021-10160-4

[66] Kokutse, N.K., Temgoua, A.G.T., Kavazović, Z. (2016). Slope stability and vegetation: Conceptual and numerical investigation of mechanical effects. Ecological Engineering, 86: 146-153. https://doi.org/10.1016/j.ecoleng.2015.11.005

[67] Zou, Z.Y., Young, M.H., Li, Z., Wierenga, P.J. (2001). Estimation of depth averaged unsaturated soil hydraulic properties from infiltration experiments. Journal of Hydrology, 242(1-2): 26-42. https://doi.org/10.1016/S0022-1694(00)00385-1

[68] Dongli, S., Dongdong, L., Yingying, Yi, L., Cuilan, X., Xin, Q., Fang, C. (2014). Profile characteristics of temporal stability of soil water storage in two land uses. Arabian Journal of Geosciences, 7: 21–34. https://doi.org/10.1007/s12517-013-0838-0\

[69] Mei, Xm., Ma, L., Zhu, Qk., Wang, S., Zhang, D., Wang, Y. (2018). Responses of soil moisture to vegetation restoration type and slope length on the loess hillslope. Journal of Mountain Science, 15: 548–562. https://doi.org/10.1007/s11629-017-4415-y

[70] Luo, Z., Fan, J., Shao, M., Hu, W., Yang, Q., Zhang, S. (2023). Soil water dynamics and groundwater evolutions of check dams under natural rainfall reduction in semi-arid areas. Journal of Hydrology, 617 (Part C): 129099. https://doi.org/10.1016/j.jhydrol.2023.129099

[71] Ya, Y., Dongdong, L., Dongli, S. (2023). Simulating the effects of vegetation restoration and climate change on the long-term soil water balance on the Loess Plateau, 2021–2050. Journal of Hydrology, 626 (Part A): 130260. https://doi.org/10.1016/j.jhydrol.2023.130260

[72] Schenk, J., Schenkels, F.A.M. (1968). Thermal free convection from an ice sphere in water. Applied Scientific Research, 19: 465–476. https://doi.org/10.1007/BF00383941

[73] Kell, G.S. (1975). Density, thermal expansivity, and compressibility of liquid water from 0" to 150°C: Correlations and tables for atmospheric pressure and saturation reviewed and expressed on 1968 temperature scale. Journal of Chemical and Engineering Data, 20(1): 97-105. https://pubs.acs.org/doi/10.1021/je60064a005

[74] Tang, A.M., Hughes, P.N., Dijkstra, T.A., Askarinejad, A., Brenčič, M., Cui, Y.J., Diez, J.J., Firgi, T., Gajewska, B., Gentile, F., Grossi, G., Jommi, C., Kehagia, F., Koda, E., ter Maat, H.W., Lenart, S., Lourenco, S., Oliveira M., Osinski, P., Springman, S.M., Stirling, R., Toll, D.G., Van Beek, V. (2018). Atmosphere–vegetation–soil interactions in a climate change context; impact of changing conditions on engineered transport infrastructure slopes in Europe. Quarterly Journal of Engineering Geology and Hydrogeology 51, 156-168. https://doi.org/10.1144/qjegh2017-103

[75] Ullah W, Ahmad K, Ullah S, Tahir AA, Javed MF, Nazir A, Abbasi AM, Aziz M, Mohammed A (2023). Analysis of the relationship among land surface temperature (LST), land use land cover (LULC), and normalized difference vegetation index (NDVI) with topographic elements in the lower Himalayan region. Heliyon, 9(e13322): 1-16. https://doi.org/10.1016/j.heliyon.2023.e13322

[76] Nunes, G. B., Portelinha, F.H.M., Futai, M.M., Yoo, C. (2022). Numerical study of the impact of climate conditions on stability of geocomposite and geogrid reinforced soil walls. Geotextiles and Geomembranes, 50(4): 807-824. https://doi.org/10.1016/j.geotexmem.2022.04.004

[77] World Weather Online. Tawang Annual Weather Averages, Arunachal Pradesh, IN https://www.worldweatheronline.com/tawang-weather-averages/arunachal-pradesh/in.aspx

[78] Hall, D.K., Martinec, J. (1985). Remote Sensing of Ice and Snow. Remote Sensing Applications (RSA), Dordrecht: Springer Netherlands.

[79] Allen, R. G., Pereira, L., Raes, D., Smith, M. (1998). Crop evapotranspiration-Guidelines for computing crop water requirements-FAO Irrigation and drainage, Paper 56.

[80] US Army Corps of Engineers. (1998). HEC-1 Flood Hydrograph Package. Hydrologic Engineering Center, (530) 756-1104. US Army Corps of Engineers, 609 Second Street, Davis, CA 95616.

[81] Burakov, D.A., Ivanova, O.I. (2010). Analysis of formation and forecast of spring snowmelt flood runoff in forest and forest-steppe basins of Siberian rivers. Russian Meteorology and Hydrology, 35: 421–431. https://doi.org/10.3103/S1068373910060099

[82] Liu, L., Sletten, R.S., Hagedorn, B., Hallet, B., McKay, C.P., Stone, J.O. (2015). An enhanced model of the contemporary and long-term (200 ka) sublimation of the massive subsurface ice in Beacon Valley, Antarctica. Journal of Geophysical Research: Earth Surface, 120(8): 1596-1610. https://doi.org/10.1002/2014JF003415

[83] Davenport, F.V., Herrera-Estrada, J.E., Burke, M., Diffenbaugh, N.S. (2019). Flood size increases nonlinearly across the Western United States in response to lower snow-precipitation ratios. Water Resources Research, 56(1): e2019WR025571. https://doi.org/10.1029/2019WR025571

[84] Ruijsch, J., Verstegen, J.A., Sutanudjaja, E.H., Karssenberg, D. (2021). Systemic change in the Rhine-Meuse basin: Quantifying and explaining parameters trends in the PCR-GLOBWB global hydrological model. Advances in Water Resources, 155: 104013. https://doi.org/10.1016/j.advwatres.2021.104013

[85] Vanapalli, S.K., Fredlund, D.G., Pufahl, D.E., Clifton, A.W. (1996). Model for the prediction of shear strength with respect to soil suction. Canadian Geotechnical Journal, 33: 379–392. http://doi.org/10.1139/t96-060

[86] Morgenstern, N.R., Price, V.E. (1965). The analysis of the stability of general slip surfaces. Géotechnique, 15: 79–93. http://doi.org/10.1680/geot.1965.15.1.79

[87] Fredlund, D.G., Krahn, J. (1977). Comparison of slope stability methods of analysis. Canadian Geotechnical Journal, 14: 429-439. https://doi.org/10.1139/t77-045

[88] IS:14243 Part-2 (1995). Selection and Development of Site for Building in Hill Areas-Guidelines. Bureau of Indian Standards, New Delhi, India.

[89] Yan, W.M., Chiu, C.F., Yuen, Ka-Ve. (2017). Prediction and modeling of permeability function and its application to the evaluation of breakthrough suction of a two-layer capillary barrier. Canadian Geotechnical Journal, 54(6): 778-788. https://doi.org/10.1139/cgj-2016-0339

[90] Yunusa, G.H., Kassim, A., Umar, M., Talib, Z.A., Abdulfatah, A.Y. (2020). Laboratory investigation of suction distribution in a modified capillary barrier system. IOP Conference Series: Earth and Environmental Science, Volume 476, 2nd International Conference on Civil & Environmental Engineering 20th - 21st November 2019, Langkawi, Kedah, Malaysia. http://doi.org/10.1088/1755-1315/476/1/012047

[91] Li, Y., Satyanaga, A., Rahardjo, H. (2021). Characteristics of unsaturated soil slope covered with capillary barrier system and deep-rooted grass under different rainfall patterns. International Soil and Water Conservation Research, 9(3): 405-418. https://doi.org/10.1016/j.iswcr.2021.03.004